



# A thalamo-amygdalar circuit underlying the extinction of remote fear memories

Bianca A. Silva<sup>ID 1,4</sup>, Simone Astori<sup>2</sup>, Allison M. Burns<sup>ID 1</sup>, Hendrik Heiser<sup>ID 1,3,5</sup>, Lukas van den Heuvel<sup>ID 1,6</sup>, Giulia Santoni<sup>1</sup>, Maria Fernanda Martinez-Reza<sup>1,7</sup>, Carmen Sandi<sup>ID 2</sup> and Johannes Gräff<sup>ID 1</sup>✉

**Fear and trauma generate some of the longest-lived memories. Despite the corresponding need to understand how such memories can be attenuated, the underlying brain circuits remain unknown. Here, combining viral tracing, neuronal activity mapping, fiber photometry, chemogenetic and closed-loop optogenetic manipulations in mice, we show that the extinction of remote (30-day-old) fear memories depends on thalamic nucleus reuniens (NRe) inputs to the basolateral amygdala (BLA). We found that remote, but not recent (1-day-old), fear extinction activates NRe-to-BLA inputs, which become potentiated upon fear reduction. Furthermore, both monosynaptic NRe-to-BLA and total NRe activity increase shortly before freezing cessation, suggesting that the NRe registers and transmits safety signals to the BLA. Accordingly, pan-NRe and pathway-specific NRe-to-BLA inhibition impairs, whereas their activation facilitates, remote fear extinction. These findings identify the NRe as a crucial BLA regulator for extinction and provide the first functional description of the circuits underlying the attenuation of consolidated fear memories.**

Traumatic events can create some of the most enduring forms of memories and lead to chronic fear and stress-related conditions, such as post-traumatic stress disorder (PTSD). The lifetime prevalence of PTSD in the general population is estimated at 7%<sup>1</sup>, and this number at least quadruples among individuals having suffered severe traumata, such as war or sexual assault<sup>1</sup>. One of the most effective measures against trauma-related disorders is a form of behavioral psychotherapy called exposure therapy<sup>2</sup>. This therapy consists of the repetitive exposure to reminders of the original traumatic memory in a safe environment, with the goal of progressively weakening the aberrant emotional responses associated with the fear-related memory<sup>3</sup>. Although exposure therapies are a reference intervention for PTSD<sup>3</sup>, they lose efficacy the later they are applied after the original traumatic experience<sup>4–6</sup>, which places strong emphasis on identifying treatment options for remote traumata<sup>7</sup>.

Using fear extinction as an experimental model of exposure therapy, previous studies in both humans and animals identified critical brain circuits that underlie fear memory attenuation<sup>8–12</sup>. However, the vast majority of these studies focused on the neural correlates of extinction protocols applied shortly after the encoding of the traumatic memory (that is, within the first day), leaving the role of extinction brain networks at remote time points poorly understood. This represents a gap in knowledge important to investigate as traumatic memories undergo a systems consolidation process over time, during which the substrates of memory storage are reorganized<sup>13,14</sup>. Therefore, fear extinction for remote memories might not rely on the same canonical brain networks as for recent time points.

## Results

Remote, but not recent, fear extinction activates an IL→NRe→BLA pathway. Previous studies on recent (that is, 1-day-old) fear memories in rodents showed that the interplay between the medial pre-frontal cortex (mPFC), in particular the infralimbic cortex (IL), and the BLA lies at the core of fear attenuation induced by exposure therapy-like extinction protocols<sup>8,9,15,16</sup>. However, the role of IL projections to the BLA (IL→BLA) has, thus far, not been investigated for remote fear memory extinction, although the BLA remains critically involved for recalling remote (that is, 30-day-old) fear memories<sup>17–19</sup> (Supplementary Fig. 1). To address this question, we combined retrograde tracing and cFos-based neuronal activity mapping to directly test the activation of IL→BLA neurons upon a previously established spaced fear extinction protocol that lastingly reduces both recent and remote contextual fear memories<sup>19,20</sup> (Fig. 1a,b). Before contextual fear conditioning (CFC), we bilaterally injected the BLA with an AAV2r-CAG::Tom (Fig. 1a,c), which infects synaptic terminals and is retrogradely transported to pre-synaptic somata<sup>21</sup>, and analyzed cFos expression in IL→BLA neurons after the last extinction session. We compared these data to control animals that did not receive shocks during the conditioning session (raw values of cFos counts and traced cells are given in Extended Data Fig. 1a–d). We found that, in contrast to recent fear memory extinction, IL→BLA-projecting neurons were not active after remote fear memory extinction (Fig. 1d,g).

To test for alternative pathways that might activate the BLA upon the extinction of remote fear memories, we screened for cFos induction in other brain areas identified by retrograde tracing<sup>21</sup>

<sup>1</sup>Laboratory of Neuroepigenetics, Brain Mind Institute, School of Life Sciences, École Polytechnique Fédérale Lausanne, Lausanne, Switzerland. <sup>2</sup>Laboratory of Behavioral Genetics, Brain Mind Institute, School of Life Sciences, École Polytechnique Fédérale Lausanne, Lausanne, Switzerland. <sup>3</sup>International Max Planck Research School “Neurosciences”, Georg-August-Universität Göttingen, Göttingen, Germany. <sup>4</sup>Present address: National Research Council of Italy, Institute of Neuroscience, Humanitas Clinical and Research Center – IRCCS, Rozzano, Milan, Italy. <sup>5</sup>Present address: Laboratory of Neural Circuit Dynamics, Brain Research Institute, University of Zürich, Zürich, Switzerland. <sup>6</sup>Present address: Laboratory of Quantitative Neurosciences, Department of Bionanoscience, Delft University of Technology, Delft, The Netherlands. <sup>7</sup>Present address: Physiological Genomics, Biomedical Center (BMC), Ludwig-Maximilians Universität München, Planegg, Germany. ✉e-mail: [johannes.graeff@epfl.ch](mailto:johannes.graeff@epfl.ch)

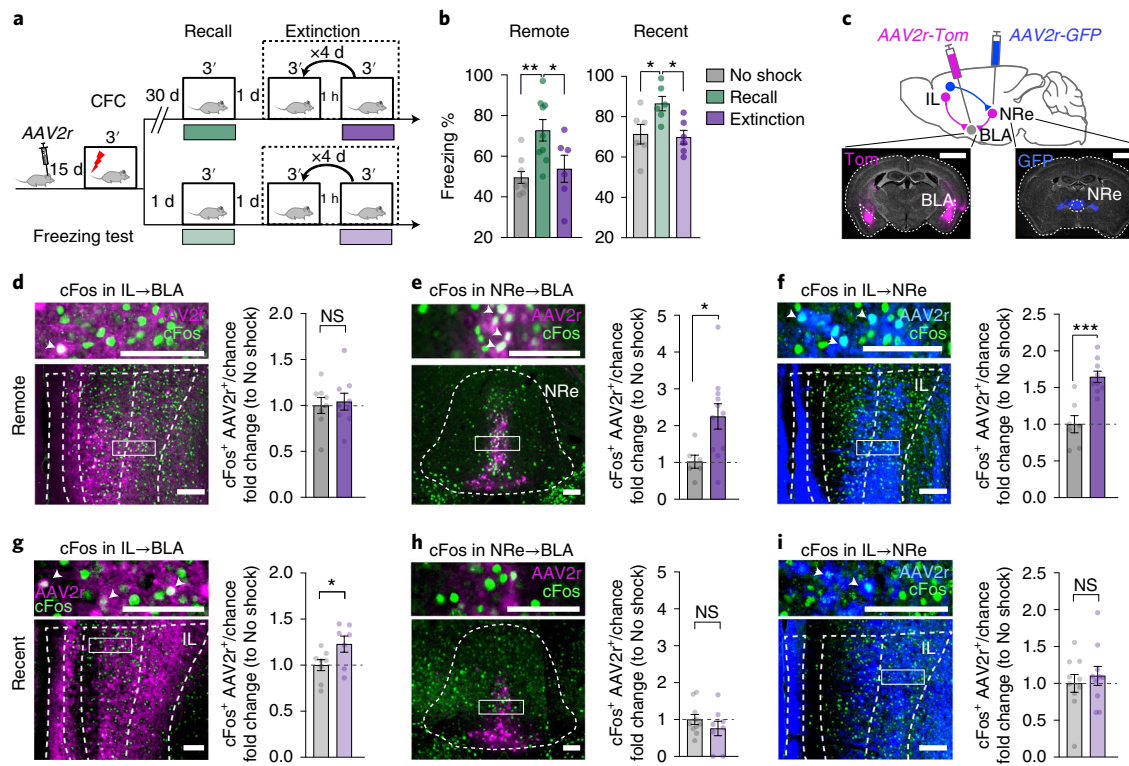


**Fig. 1 | Remote fear extinction recruits an IL→NRe→BLA pathway.** **a**, Schematic of the behavioral paradigm. Thirty days (remote, top) or 1 d (recent, bottom) after CFC, animals were re-exposed to the conditioned context in the absence of foot shock (Recall) and, subsequently, to the spaced fear extinction paradigm consisting of two daily sessions of context exposure for 4 d. Control animals did not receive foot shocks during conditioning but underwent the extinction procedure (No shock). **b**, Freezing during recall and the last extinction session (Extinction) of the remote (left) and recent (right) fear memory extinction paradigm compared to control animals. Remote: one-way ANOVA,  $F_{2,21} = 7.13$ ,  $P = 0.004$ , multiple comparison, Holm-Sidak, \* $P < 0.05$ , \*\* $P < 0.01$ ; Recent: one-way ANOVA,  $F_{2,15} = 5.32$ ,  $P = 0.018$ , multiple comparison, Holm-Sidak, \* $P < 0.05$ , \*\* $P < 0.01$ .  $n = 6\text{--}10$  animals per behavioral group. **c**, Schematic representation (top) and example pictures (bottom) of the retrograde virus injection strategy. Scale bar, 1 mm.

**d-f**, Representative picture (left) and co-localization analysis (right) in the remote extinction group and the No shock control group of retrogradely traced cells from the BLA (AAV2r+) active (cFos+) in the IL (**d**) (unpaired  $t$ -test,  $P = 0.748$ ,  $n = 8$  (No shock) and 9 (Ext) mice per behavioral group); of retrogradely traced cells from the BLA (AAV2r+) active (cFos+) in the NRe (**e**) (unpaired  $t$ -test,  $P = 0.024$ ,  $n = 6$  (No shock) and 11 (Ext) mice per behavioral group); and of retrogradely traced cells from the NRe (AAV2r+) active (cFos+) in the IL (**f**) (unpaired  $t$ -test,  $P = 0.0003$ ,  $n = 7$  (No shock) and 9 (Ext) mice per behavioral group). **g-i**, Representative picture (left) and co-localization analysis (right) in the recent extinction group and the No shock control group of retrogradely traced cells from the BLA (AAV2r+) active in the IL (cFos+) (**g**) (unpaired  $t$ -test,  $P = 0.0459$ ,  $n = 8$  (No shock) and 7 (Ext) mice per behavioral group); of retrogradely traced cells from the BLA (AAV2r+) active (cFos+) in the NRe (**h**) (unpaired  $t$ -test,  $P = 0.31$ ,  $n = 10$  (No shock) and 8 (Ext) mice per behavioral group); and of retrogradely traced cells from the NRe (AAV2r+) active (cFos+) in the IL (**i**) (unpaired  $t$ -test,  $P = 0.57$ ,  $n = 10$  mice per behavioral group). Scale bar, 100 μm. **d-i**, Arrowheads indicate double-positive cells (AAV2r+ cFos+). Data are represented as mean ± s.e.m. Statistical analysis details for each figure panel are reported in Supplementary Table 1. Ext, extinction; NS, not significant.

(Extended Data Fig. 2a,b). We found that BLA-projecting neurons in the NRe of the thalamus (Fig. 1e; for precise definition of NRe boundaries, see Methods) and the ventral tegmental area (VTA; Extended Data Fig. 2c-f) were activated upon remote fear extinction. Because the NRe was previously implicated as an important hub for the consolidation of remote memories<sup>22–24</sup>, we reasoned that it might have a similar role for their extinction and serve as a node between the IL and BLA. To test this hypothesis, we injected a retrogradely transported virus in the NRe (AAV2r-CAG::GFP; Fig. 1c) and assessed cFos activation in IL→NRe projections upon remote fear memory extinction. We found increased cFos activation in the IL→NRe neuronal population after remote fear memory extinction (Fig. 1f), which was largely non-overlapping with IL→BLA neurons (Supplementary Fig. 2), suggesting that fear extinction induces activation of different IL outputs with memory age. Notably, these AAV2 retrograde tracing results were confirmed by anterograde tracing (Supplementary Fig. 3) and by pseudotyped rabies-based tracing of inputs and outputs (TRIO)<sup>25</sup> (Extended Data Fig. 3).

Conversely, when we analyzed IL→NRe and NRe→BLA activation upon recent fear memory extinction, we found no cFos increase in either of these projections (Fig. 1h,i and Extended Data Fig. 1e). Together, these results suggest that the circuits supporting fear extinction undergo a functional switch as memories age and posit the NRe to be implicated in remote fear memory extinction.

**NRe activity bidirectionally modulates remote fear extinction.** To test whether the NRe is directly participating in remote fear memory extinction, we next manipulated its activity during this process. To this end, we first inhibited NRe neurons by expressing the inhibitory designer receptor exclusively activated by designer drug (DREADD) hM4Di via stereotaxic NRe injections of an AVV8-hSyn::hM4Di-mCherry (Fig. 2a), followed by daily clozapine N-oxide (CNO, the DREADD agonist) administration at remote memory recall and during the extinction paradigm (Fig. 2b). We found that, as the extinction protocol proceeded, CNO-treated animals retained significantly higher freezing levels

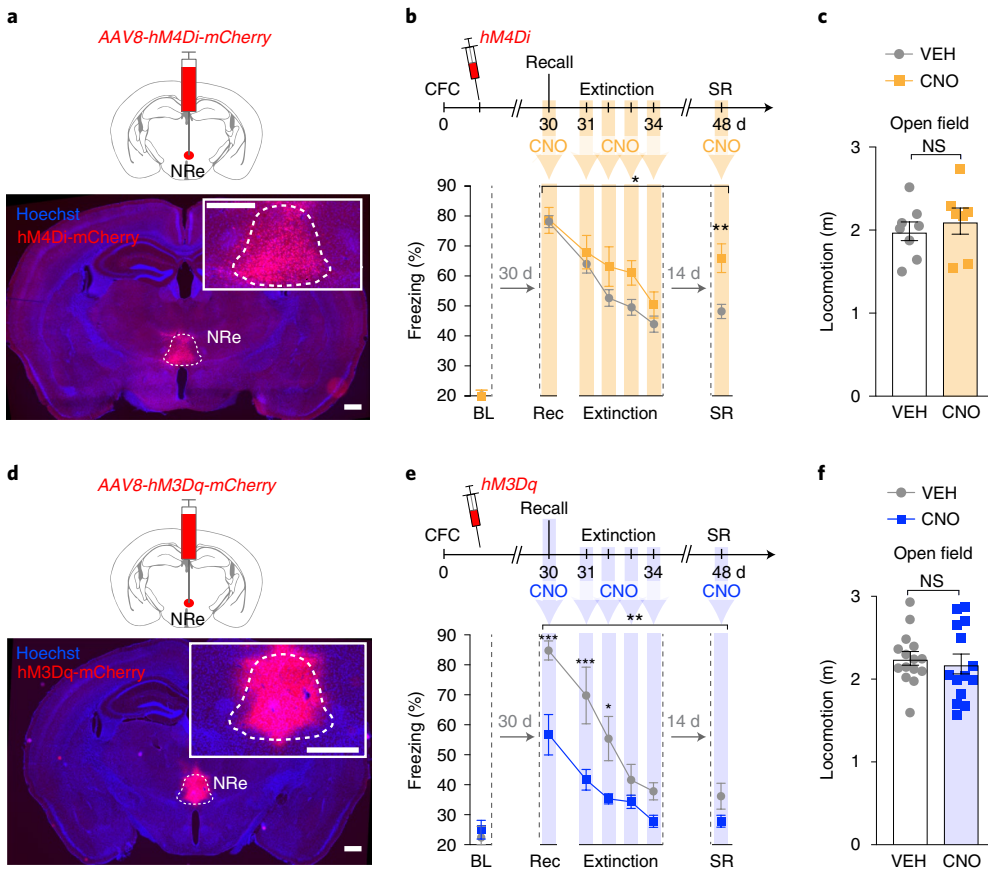


**Fig. 2 | The NRe bidirectionally modulates remote fear memory extinction.** **a**, Top: schematic representation of AAV8-hM4Di-mCherry injection in the NRe. Bottom: representative picture of hM4Di-mCherry expression in the NRe. Scale bar, 500  $\mu$ m. **b**, Top: experimental timeline. All animals underwent CFC and were injected with AAV8-hSyn::hM4Di-mCherry 1 week later. Thirty days after CFC, the animals underwent memory recall, the spaced extinction procedure and a test for spontaneous recovery of the fear (SR) under CNO or vehicle treatment (VEH). Bottom: freezing responses during the remote fear memory extinction paradigm and SR upon hM4Di/CNO-mediated inhibition of the NRe or its vehicle control. Yellow bars indicate days of CNO or VEH administration. Two-way repeated-measures ANOVA, VEH versus CNO:  $F_{1,45} = 5.696$ ,  $P = 0.02$ , Sidak's multiple comparison, \*\* $P < 0.01$ ,  $n = 10$  (CNO) and 37 (VEH) mice per group. **c**, Locomotion analysis in an open field arena upon hM4Di/CNO-mediated inhibition of the NRe. Unpaired  $t$ -test,  $P = 0.53$ .  $n = 7$  (CNO) and 8 (VEH) mice per group. **d**, Top: schematic representation of AAV8-hM3Dq-mCherry injection in the NRe. Bottom: representative picture of hM3Dq-mCherry expression in the NRe. Scale bar, 500  $\mu$ m. **e**, Top: experimental timeline. All animals underwent CFC and were injected with AAV8-CamKII::hM3Dq-mCherry 1 week later. Thirty days after CFC, the animals underwent memory recall, the spaced extinction procedure and an SR test under CNO or VEH treatment. Bottom: freezing responses during the remote fear memory extinction paradigm and SR upon hM3Dq-mediated activation of the NRe. Blue bars indicate days of CNO or VEH exposure. Two-way repeated-measures ANOVA, VEH versus CNO:  $F_{1,9} = 14.01$ ,  $P = 0.0046$ , Sidak's multiple comparison, \* $P < 0.05$ , \*\* $P < 0.01$ , \*\*\* $P < 0.001$ ,  $n = 5$  (VEH) and 6 (CNO) mice per behavioral group. **f**, Locomotion analysis in an open field arena upon hM3Dq-mediated activation of the NRe. Unpaired  $t$ -test,  $P = 0.64$ ,  $n = 14$  (CNO) and 15 (VEH) mice per group. Data are represented as mean  $\pm$  s.e.m. Statistical analysis details for each figure panel are reported in Supplementary Table 1. BL, baseline freezing upon novel context exposure; NS, not significant; Rec, recall.

than vehicle-treated animals (Fig. 2b). This effect was also visible when the animals were tested for spontaneous recovery (SR) of fear with a context re-exposure 14 d later, pointing to a persistent impairment of fear extinction upon NRe inactivation. Moreover, NRe inhibition during the extinction phase alone yielded a similar impairment of fear attenuation even upon CNO-free context exposure 14 d later (Extended Data Fig. 4a). In contrast, acute inhibition of the NRe only at SR did not affect freezing behavior (Extended Data Fig. 4b), suggesting that the NRe plays a crucial role in extinction learning but not in extinction memory retrieval. Furthermore, CNO administration did not affect fear extinction in animals with off-target hM4Di-mCherry expression (that is, with hM4Di expression outside the NRe; Extended Data Fig. 4c,d), which argues against unspecific CNO effects. Lastly, we observed no differences upon hM4Di-mediated NRe inhibition in overall locomotor activity

in an open field test (Fig. 2c), indicating that the elevated freezing observed during the extinction paradigm was not due to an unspecific increase in immobility. Thus, a loss of function of NRe activity impairs remote fear memory extinction.

Next, we evaluated whether a gain of function of NRe activity might be beneficial for remote fear memory extinction. For this, we expressed the activatory DREADD hM3Dq in excitatory NRe neurons by stereotaxic injections of AAV8-CamKII::hM3Dq-mCherry (Fig. 2d), which, upon systemic administration of CNO, induced activation in hM3Dq-mCherry-transduced NRe neurons as revealed by cFos immunohistochemistry (IHC) (Extended Data Fig. 5a,b). We found that CNO-mediated NRe activation during memory recall and each of the extinction sessions resulted in decreased freezing starting from the first context re-exposure (Fig. 2e). Notably, chemogenetic NRe activation performed during extinction alone

elicited similarly facilitated fear reduction (Extended Data Fig. 5c). Conversely, the same NRe activation protocol performed in the home cage, but in the absence of extinction training, did not alter the animals' freezing response upon context re-exposure 1 d or 14 d later (Extended Data Fig. 5d). Furthermore, chemogenetic NRe activation did not affect overall locomotor activity (Fig. 2f), excluding the possibility that changes in freezing responses were secondary to locomotor effects. These findings indicate that increasing NRe activity during extinction training facilitates fear memory attenuation.

**NRe activity increases upon freezing cessation during remote extinction.** To gain insight into the real-time activity of the NRe and its relation with the online freezing state of the animals during remote fear memory extinction, we next performed *in vivo* fiber photometry recordings in the NRe. To this end, we expressed the genetically encoded  $\text{Ca}^{2+}$  indicator GCaMP6f in NRe excitatory neurons by local injection of *AAV1-CamKII::GCaMP6f* and recorded  $\text{Ca}^{2+}$ -dependent and  $\text{Ca}^{2+}$ -independent fluorescence via an optical fiber implant at the injection site, through which we simultaneously delivered 465 nm and 405 nm of excitation light<sup>26</sup> (Fig. 3a). Using a within-subject design, we compared NRe activity between context exposure before fear conditioning ('Habituation'), at memory recall 30 d after conditioning ('Recall') and during each session of the spaced extinction protocol ('Extinction'), which expectedly reduced remote fear memories (Fig. 3b,c).

Upon temporal alignment of the photometry traces to freezing epochs, we observed a transient elevation in NRe activity starting shortly before the termination of freezing bouts during both recall and each of the extinction sessions (Fig. 3d and Extended Data Fig. 6a). Of note, this activation was not observed upon cessation of immobility bouts during habituation, showing it to be specifically related to fear responses (Fig. 3d). Furthermore, such dF/F transients were absent in the 405-nm traces, indicating that they were selectively related to  $\text{Ca}^{2+}$  signals and not to fiber motion artifacts. dF/F quantifications across subjects confirmed the significant NRe activity increase upon freezing cessation during the recall and last extinction session but not during habituation (Fig. 3e,f). This increase in NRe activity was initiated approximately 500 ms before freezing termination, was most prominent around 200 ms before (Fig. 3g-i) and was not correlated with freezing initiation (Extended Data Fig. 6b,c). These findings show that NRe activity increases are time-locked to freezing cessation.

**NRe activity mediates freezing cessation during remote extinction.** To test whether such increase in NRe activity preceding freezing cessation could play a causal role in modulating freezing duration during remote fear memory extinction, we next manipulated the activity of NRe excitatory neurons time-locked to freezing using a behavioral closed-loop optogenetic approach. For this, we coupled an online freezing detection system to a laser driver, so that photostimulation could be specifically triggered upon freezing (Fig. 4a). First, we used an optogenetic gain-of-function approach in animals expressing the activatory opsin Chronos in NRe excitatory neurons (achieved by the combined NRe injection of *AAV1-CamKII::Cre* and *AAV1-FLEX-Chronos-GFP* or its control *AAV1-FLEX-GFP*; Fig. 4b), which reliably induced action potentials at increasing stimulation frequencies (up to 20 Hz) as revealed by *ex vivo* slice recordings (Supplementary Fig. 4a). When we applied the behavioral closed-loop photo-excitation of the NRe during remote fear memory extinction, we observed a shorter duration of freezing bouts (Fig. 4c) and an overall reduced latency to freezing cessation (Fig. 4d,e). These data indicate that an optogenetic stimulation of the NRe that mimicks its naturally occurring increase upon freezing cessation facilitates fear attenuation.

To confirm these findings, we employed a behavioral closed-loop optogenetic inhibition approach by expressing the inhibitory opsin

ArchT in NRe excitatory neurons (achieved by combined viral injections of *AAV1-CamKII::Cre* and *AAV1-FLEX-ArchT-GFP* into the NRe or its control *AAV1-FLEX-GFP*) (Fig. 4f,g). When the NRe was photo-inhibited each time a freezing bout was detected during the extinction paradigm, we found an increased duration of freezing bouts (Fig. 4h) and an overall greater latency to freezing cessation (Fig. 4i,j). Together, these results indicate that NRe activity plays a crucial role in mediating the termination of freezing bouts during remote fear memory extinction.

#### Time-locked NRe→BLA activity regulates freezing cessation.

Next, we investigated how the NRe→BLA pathway, found to be activated upon remote fear memory extinction (Fig. 1e), might regulate this process. We first characterized the NRe→BLA connection in comparison to other known NRe outputs<sup>27</sup>. To this end, we injected animals with *AAV8-CamKII::hM3Dq-mCherry* in the NRe and, 90 min after CNO administration, measured cFos expression in the mPFC, hippocampal area CA1 and the amygdala, which showed prominent mCherry<sup>+</sup> fiber density (Extended Data Fig. 7a). Of these, we found that only the BLA and lateral portion of the central amygdala (CeAl) were activated after chemogenetic NRe stimulation (Extended Data Fig. 7b,c).

Subsequently, we further characterized these amygdalar output regions of the NRe by optogenetic circuit mapping. For this, we virally transduced the NRe with an *AAV1-hSyn::Chronos-Tom* (Extended Data Fig. 7d) and performed *ex vivo* whole-cell recordings in the CeA and in principle neurons located in the BLA and the lateral amygdala (LA). Photostimulation of NRe fibers elicited excitatory post-synaptic currents (EPSCs) in all amygdalar sub-regions, but the responses were significantly (on average >10 times) larger in the BLA than in the CeA and LA (Extended Data Fig. 7e). EPSCs in BLA neurons also displayed lower paired-pulse ratio than in the CeA and the LA, indicating higher release probability at NRe terminals innervating the BLA (Extended Data Fig. 7f). These results confirm NRe→BLA projectors as a major output connection of the NRe.

Next, we assessed the real-time engagement of this NRe→BLA pathway during remote fear memory extinction by pathway-specific *in vivo* fiber photometry. To do so, we injected a retrogradely transported virus carrying Cre in the BLA (*AAV2r-pgk::Cre*) and a Cre-dependent GCaMP6f expressing virus (*AAV1-hSyn::FLEX-GCaMP6f*) in the NRe (Fig. 5a). We observed increased NRe→BLA activity before the end of freezing bouts during the recall and extinction sessions but not before the end immobility bouts during habituation (Fig. 5b,c), in accordance with cFos mapping results at these time points (Extended Data Fig. 8). In line with the pan-NRe *in vivo* fiber photometry recordings (Fig. 3d,e), this finding suggests that, during remote fear memory extinction, NRe→BLA projectors are specifically activated upon freezing cessation.

To test whether such increased activity in NRe→BLA neurons preceding freezing cessation can modulate freezing behavior during remote fear extinction, we then employed a pathway-specific behavioral closed-loop optogenetic stimulation protocol, analogous to the one used in Fig. 4a. We injected a retrogradely transported virus carrying Cre in the BLA (*AAV2r-pgk::Cre*) and a Cre-dependent Chronos-expressing virus (*AAV1-hSyn::FLEX-Chronos-GFP* or its control *AAV1-hSyn::FLEX-GFP*) in the NRe and stimulated NRe→BLA neurons time-locked to freezing behavior (Fig. 5d,e). Photostimulation of Chronos-expressing NRe terminals reliably induced post-synaptic currents at increasing stimulation frequencies (up to 20 Hz) in the BLA, as revealed by *ex vivo* slice recordings (Supplementary Fig. 4b). We found that closed-loop optogenetic stimulation of NRe→BLA neurons during remote fear memory extinction led to a decreased duration of freezing bouts as compared to control animals (Fig. 5e) and to an overall reduced latency to

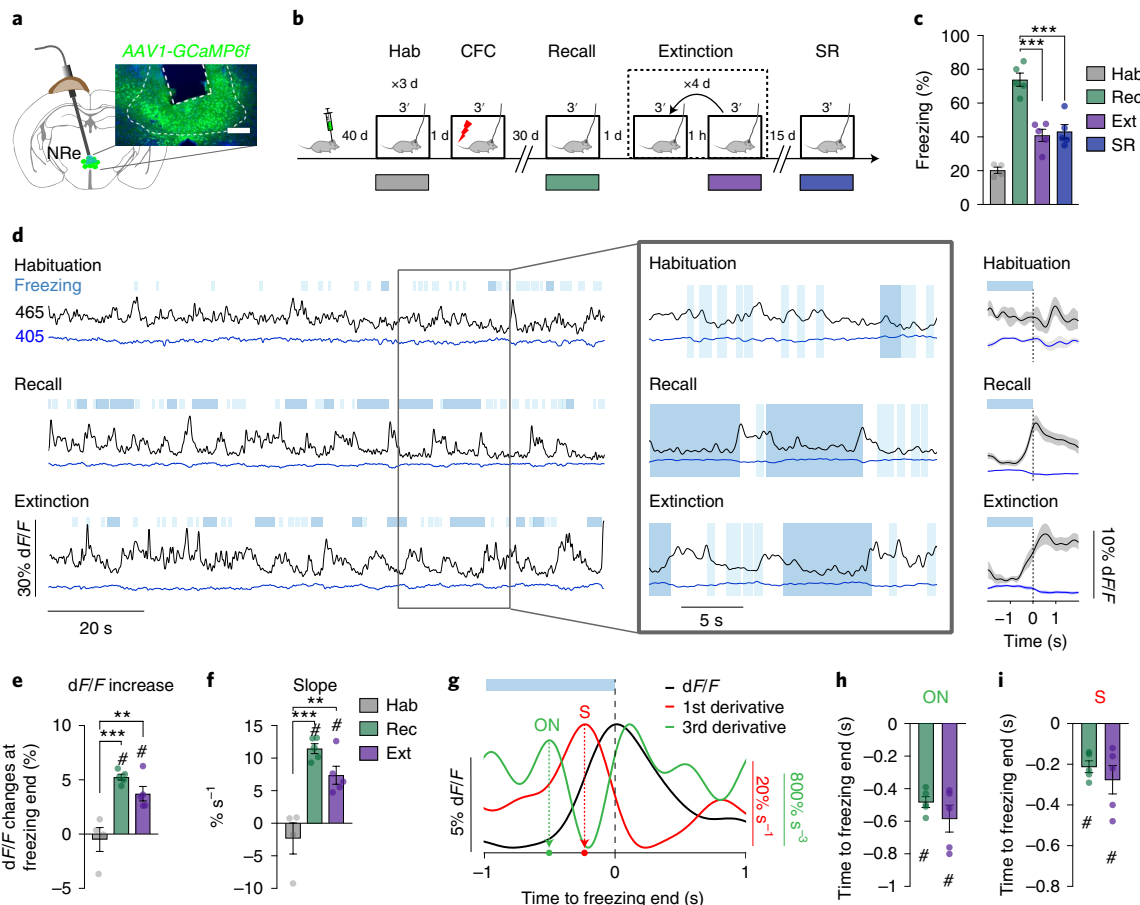


**Fig. 3 |** Freezing cessation during remote fear memory recall and extinction is preceded by increased NRe activity. **a**, Schematic (left) and representative picture (right) of the fiber photometry implant and GCaMP6f expression in the NRe. Scale bar, 200  $\mu$ m. **b**, Schematic of the experimental setup. Forty days after fiber optic implantation, animals were habituated (Hab) to the context and connected to the patch cord once per day for 3 d and underwent CFC 1 d later. Thirty days after, they were exposed to the conditioned context in the absence of foot shock (Recall) and, subsequently, to the spaced extinction paradigm. Fifteen days later, animals received another context exposure to test for the spontaneous recovery of fear (SR). **c**, Freezing during Habituation, Recall, the last extinction session (Ext) and SR. One-way repeated-measures ANOVA for Rec, Ext and SR,  $F_{2,8} = 31.1$ ,  $P = 0.0002$ , Sidak's multiple comparison, \*\*\* $P < 0.001$ .  $n = 5$  animals. **d**, Left: example traces of photometry signals (reported as  $dF/F$ ; Methods) generated by 465-nm (black,  $Ca^{2+}$ -dependent) and 405-nm (blue,  $Ca^{2+}$ -independent) LED excitation during Habituation, Recall and the last Ext session. Blue boxes above the traces indicate freezing bouts ( $0.5 s \geq$  light blue  $< 1.5 s$ ; dark blue  $\geq 1.5 s$ ). Boxed, expanded portions of the traces on the left, relating NRe activity and freezing bouts. Right: mean  $dF/F$  signal  $\pm 2$  s around freezing cessation (dashed line, 0 s) for  $\geq 1.5$ -s freezing bouts from the corresponding behavioral session. **e**, Quantification of  $dF/F$  difference before and after freezing end. One-way ANOVA,  $F_{2,11} = 16.96$ ,  $P = 0.0004$ , Sidak's multiple comparison, \*\* $P < 0.01$ , \*\*\* $P < 0.001$ ,  $n = 4$  (Hab) and 5 (Recall and Ext) mice per time point. Two-tailed one-sample  $t$ -test (theoretical mean = 0), # $P < 0.01$ ,  $n = 4$ –5 animals per time point. **f**, Quantification of  $dF/F$  mean slope during the 0.4-s interval before freezing end. One-way ANOVA,  $F_{2,11} = 20.25$ ,  $P = 0.0002$ , Sidak's multiple comparison, \*\* $P < 0.01$ , \*\*\* $P < 0.001$ ,  $n = 4$  (Hab) and 5 (Recall and Ext) mice per time point. Two-tailed one-sample  $t$ -test (theoretical mean = 0), # $P < 0.01$ ,  $n = 4$  (Hab) and 5 (Recall and Ext) mice per time point. **g**, Illustration of the first and third derivative of mean  $dF/F$  around freezing end used to calculate signal onset (ON) and latency of steepest rise (S) relative to freezing cessation (dashed line, 0 s). **h**, Quantification of signal onset latency to freezing end. Two-tailed one-sample  $t$ -test (theoretical mean = 0), # $P < 0.01$ ,  $n = 5$  animals per time point. **i**, Quantification of steepest rise latency to freezing end. Two-tailed one-sample  $t$ -test (theoretical mean = 0), # $P < 0.05$ ,  $n = 5$  animals per time point. Data are represented as mean  $\pm$  s.e.m. Statistical analysis details for each figure panel are reported in Supplementary Table 1. Rec, recall.

freezing cessation (Fig. 5f,g). This result indicates that NRe  $\rightarrow$  BLA activity can directly induce termination of freezing bouts during remote fear memory extinction.

**NRe  $\rightarrow$  BLA synaptic plasticity reflects remote fear extinction.** The observation that activity in NRe  $\rightarrow$  BLA-projecting neurons is tightly related to freezing cessation throughout the remote fear extinction paradigm indicates that this pathway might be a major input to the BLA to encode remote fear extinction. To assess this, we first probed whether NRe  $\rightarrow$  BLA connections undergo synaptic plasticity after efficient remote fear extinction by measuring the AMPA/NMDA EPSC ratio<sup>28</sup> in this pathway. We virally transduced the NRe with

an AAV1-hSyn::Chronos-Tom and patched BLA neurons receiving inputs from the NRe ex vivo 1 d after the last extinction session (Fig. 6a,b). We found that remote fear memory extinction was accompanied by a significant increase in AMPA/NMDA ratio in the BLA, compared to remote fear recall alone and to control animals that either did not undergo extinction or did not receive foot shocks during conditioning but were exposed to the extinction procedure (Fig. 6c). Notably, such increase in AMPA/NMDA ratio was not observed for recent fear memory extinction (Supplementary Fig. 5), in line with a lack of NRe  $\rightarrow$  BLA activation at this time point (Fig. 1h). This finding shows that remote fear memory extinction specifically leads to synaptic potentiation of NRe  $\rightarrow$  BLA inputs.

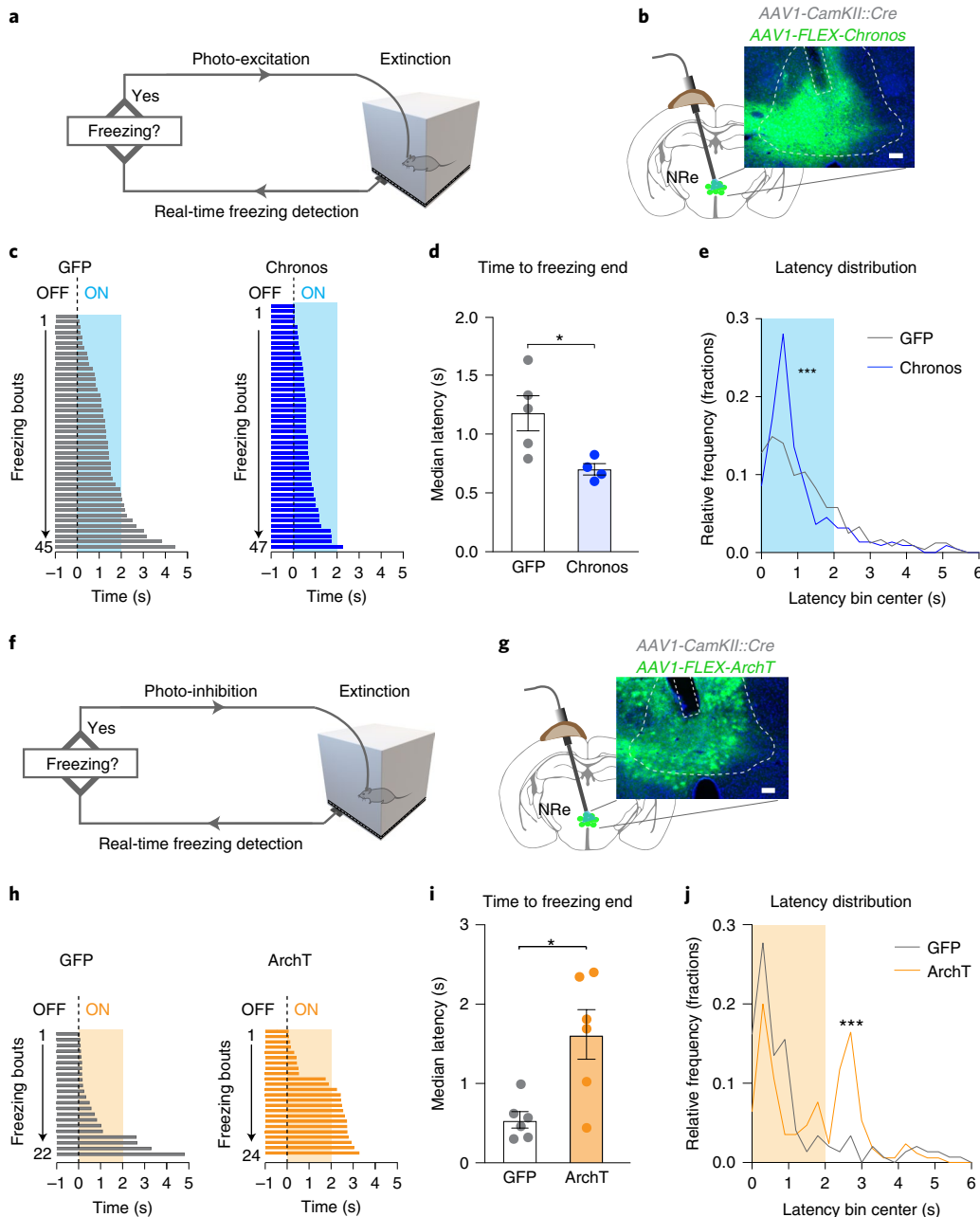


**Fig. 4 | Behavioral closed-loop optogenetic manipulation of the NRe during remote fear memory extinction bidirectionally modulates freezing cessation.**

**a**, Schematic representation of the behavioral closed-loop optogenetic activation experimental strategy: real-time freezing detection triggers NRe photostimulation (20 Hz, 2 s) after each freezing bout of  $\geq 1$ s. **b**, Left: schematic representation of the optogenetic fiber optic implant; right: representative picture of Chronos-GFP expression in NRe excitatory neurons achieved by co-infection of an AAV1-CamKII::Cre and AAV1-Syn::FLEX-Chronos-GFP and localization of the optical fiber implant in the NRe. Scale bar, 100  $\mu$ m. **c**, Example of freezing cessation upon NRe photostimulation (blue shading) in an AAV1-GFP-injected (left) and AAV1-Chronos-GFP-injected (right) animal. Freezing bouts are ordered by freezing epoch duration. **d**, Latency to freezing cessation upon NRe behavioral closed-loop optogenetic stimulation in AAV1-GFP- and AAV1-Chronos-GFP-injected animals. Two-tailed t-test (Welch-corrected),  $P=0.03$ ,  $n=4$  (Chronos), 5 (GFP) mice per group. **e**, Distribution analysis of latency to freezing cessation from light stimulation onset in AAV1-GFP- and AAV1-Chronos-GFP-injected animals (bin width, 300 ms); Kolmogorov-Smirnov test,  $P=0.0007$ ,  $n=221$  (Chronos), 242 (GFP) latencies per behavioral group, 4–5 animals per group. **f**, Schematic representation of the behavioral closed-loop optogenetic inhibition experimental strategy. Real-time freezing detection triggers NRe photo-inhibition (continuous, 2 s) after each freezing bout of  $\geq 1$ s. **g**, Left: schematic representation of the optogenetic fiber optic implant; right: representative picture of ArchT-GFP expression in NRe excitatory neurons achieved by co-infection of an AAV1-CamKII::Cre and AAV1-Syn::FLEX-ArchT-GFP and localization of the optical fiber implant in the NRe. Scale bar, 100  $\mu$ m. **h**, Example of freezing cessation upon NRe photo-inhibition (orange shading) in an AAV1-GFP-injected (left) and AAV1-ArchT-GFP-injected (right) animal. Freezing bouts are ordered by freezing epoch duration. **i**, Latency to freezing cessation upon NRe behavioral closed-loop optogenetic inhibition in AAV1-GFP- and AAV1-ArchT-GFP-injected animals. Two-tailed t-test (Welch-corrected),  $P=0.017$ ,  $n=6$  mice per group. **j**, Distribution analysis of latency to freezing cessation from light stimulation onset in AAV1-GFP- and AAV1-ArchT-GFP-injected animals (bin width, 300 ms); Kolmogorov-Smirnov test,  $P<0.0001$ ,  $n=148$  (GFP), 170 (ArchT) latencies per behavioral group, 6 animals per group. Data in bar charts are represented as mean  $\pm$  s.e.m. Statistical analysis details for each figure panel are reported in Supplementary Table 1.

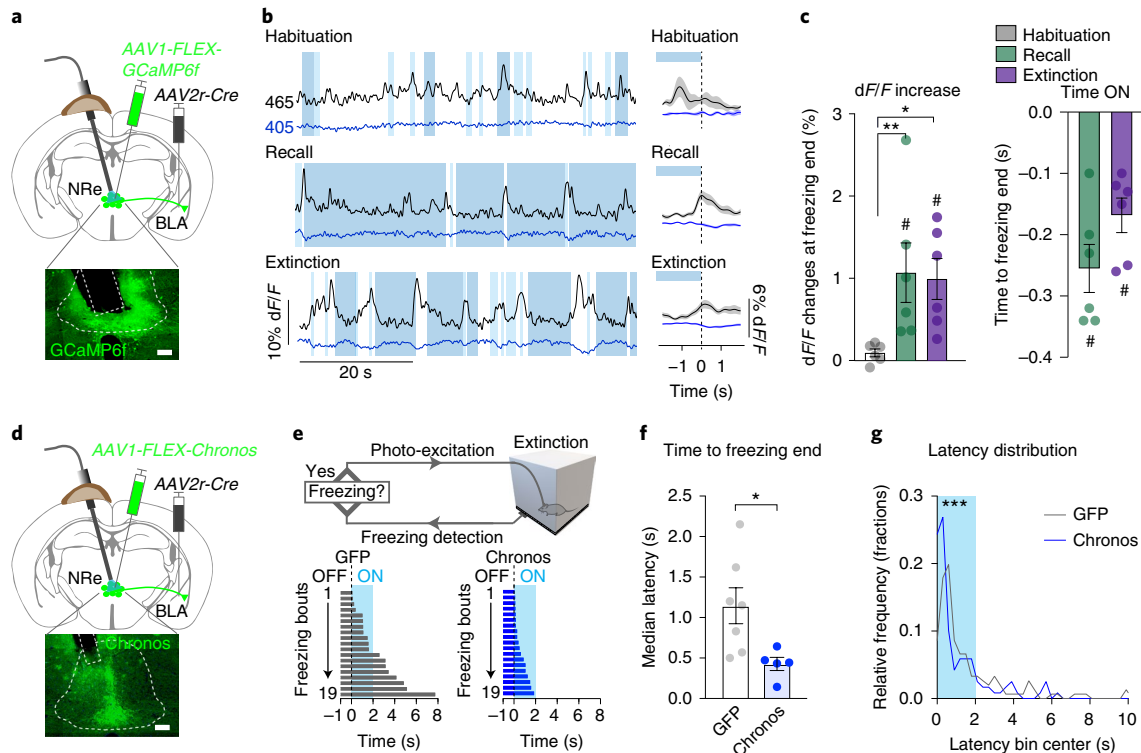
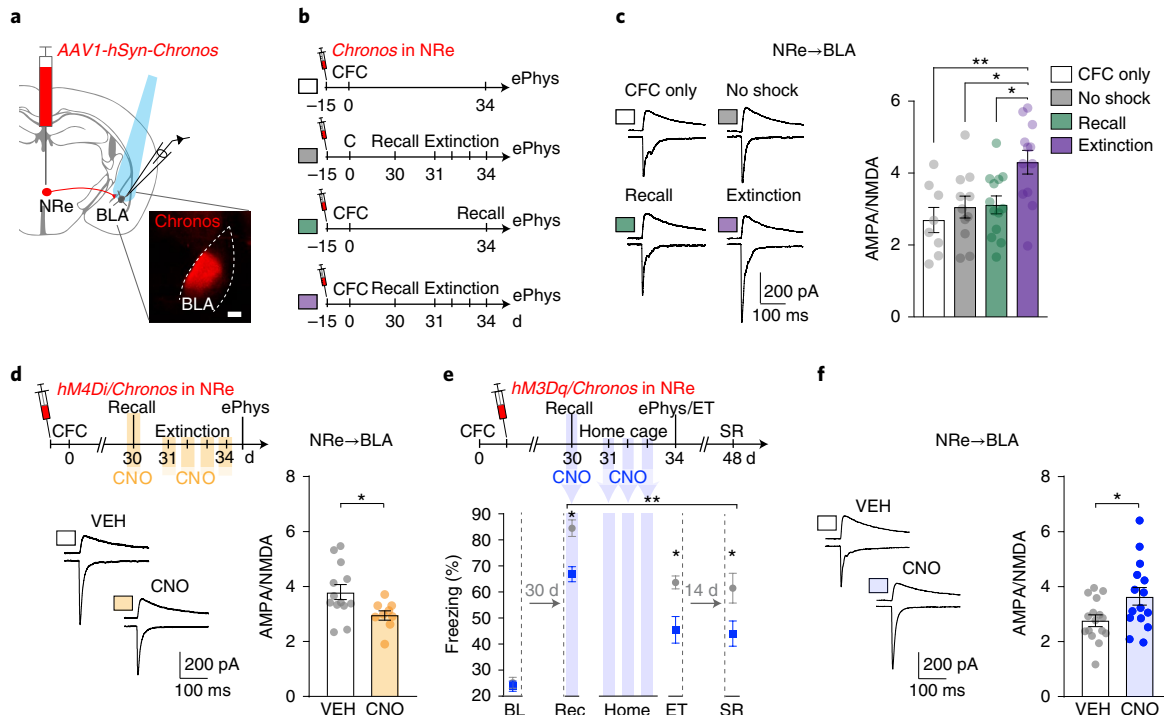


**Fig. 5 | NRe projections to the BLA are recruited upon and regulate freezing cessation during remote extinction.** **a**, Top: schematic of the experimental approach and fiber photometry recording implant; bottom: representative picture of GCaMP6f expression and localization of the optical fiber implant in the NRe. Scale bar, 100  $\mu$ m. **b**, Left: example traces of photometry signals (reported as dF/F; Methods) generated by 465-nm (black,  $\text{Ca}^{2+}$ -dependent) and 405-nm (blue,  $\text{Ca}^{2+}$ -independent) LED excitation during Habituation (Hab), Recall and the last extinction (Ext) session. Blue boxes indicate freezing bouts ( $0.5\text{s} \geq \text{light blue} < 1.5\text{s}$ ; dark blue  $\geq 1.5\text{s}$ ). Right: mean dF/F signal  $\pm 2\text{s}$  around cessation of freezing (indicated by the dashed line, 0 s) for  $\geq 1.5\text{s}$  freezing bouts from the corresponding behavioral session on the left. **c**, Left: quantification of dF/F difference before and after freezing end. Repeated-measures one-way ANOVA,  $F_{2,10} = 7.99$ ,  $P = 0.0084$ , multiple comparison, Holm-Sidak, \* $P < 0.05$ , \*\* $P < 0.01$ ,  $n = 6$  animals. Two-tailed one-sample t-test (theoretical mean = 0), # $P < 0.05$ ,  $n = 6$  animals. Right: quantification of steepest rise latency relative to freezing end. Two-tailed one-sample t-test (theoretical mean = 0), # $P < 0.01$ ,  $n = 6$  animals per time point. **d**, Top: schematic representation of the NRe→BLA pathway-specific optogenetic stimulation strategy and fiber optic implant; bottom: representative picture of Chronos-GFP expression in NRe neurons projecting to the BLA and localization of the optical fiber implant in the NRe. Scale bar, 100  $\mu$ m. **e**, Top: schematic representation of the behavioral closed-loop optogenetic activation experimental strategy. During experimental extinction, real-time freezing detection triggers NRe photostimulation (20 Hz, 2 s) after each freezing bout of  $\geq 1\text{s}$ . Bottom: example of freezing cessation upon NRe→BLA photostimulation (blue shading) in an AAV1-GFP-injected (control, left) and an AAV1-Chronos-GFP-injected (right) animal. Freezing bouts are ordered by freezing epoch duration. **f**, Latency to freezing cessation upon NRe→BLA behavioral closed-loop optogenetic stimulation in AAV1-GFP- and AAV1-Chronos-GFP-injected animals. Two-tailed t-test (Welch-corrected),  $P = 0.017$ ,  $n = 5$  (Chronos) and 7 (GFP) animals per group. **g**, Distribution analysis of latency to freezing cessation from light stimulation onset in AAV1-GFP- and AAV1-Chronos-GFP-injected animals in NRe→BLA neurons (bin width, 300 ms); Kolmogorov-Smirnov test,  $P = 0.0005$ ,  $n = 119$  (Chronos) and 151 (GFP) latencies per behavioral group (5–7 animals per group). Data are represented as mean  $\pm$  s.e.m. Statistical analysis details for each figure panel are reported in Supplementary Table 1.

We then tested whether reduced synaptic potentiation in the NRe→BLA pathway might underlie fear extinction impairments. To this end, we measured the AMPA/NMDA ratio of NRe→BLA connections 1 d after the remote fear memory extinction paradigm performed under NRe chemogenetic inhibition, which prevented efficient fear memory extinction (Fig. 6b). In comparison to vehicle-treated animals showing efficient memory extinction, we found blunted AMPA/NMDA ratio when the NRe activity was inhibited during extinction (Fig. 6d, lower panel). This finding implies that an impairment of remote fear memory extinction is reflected by reduced synaptic plasticity in NRe→BLA outputs.

Next, we assessed whether artificially activating the NRe might induce such plasticity and ameliorate remote fear memory extinction. For this purpose, we employed a suboptimal fear extinction protocol, in which animals received only a single context re-exposure (recall) 30 d after CFC, followed by no extinction training (that is, the animals remained untested in their home cage on the subsequent days; Fig. 6e, upper panel). This protocol only

partially reduced the animals' fear response as revealed by a test for their 'extinction memory' the day after (VEH-treated animals in Fig. 6e). Correspondingly, this protocol did not induce plasticity in the NRe→BLA pathway (VEH-treated animals in Fig. 6f), which showed similar AMPA/NMDA levels to control animals that did not undergo extinction at all (Fig. 6c). Conversely, when we repeatedly stimulated NRe activity by daily CNO administration, even in the absence of extinction training, we observed increased AMPA/NMDA ratio in NRe→BLA projectors (CNO-treated animals in Fig. 6f). Notably, such artificially induced potentiation was reflected by decreased freezing levels when the animals were tested for their 'extinction memory' using the same behavioral paradigm (CNO-treated animals in Fig. 6e). This reduction of the freezing response was maintained even when the animals were tested for SR 14 d later in the absence of CNO (Fig. 6e). Conversely, no fear reduction was observed when NRe activity was stimulated only once (Supplementary Fig. 6) or when repeated NRe stimulation was performed in the absence of context re-exposure (Extended Data



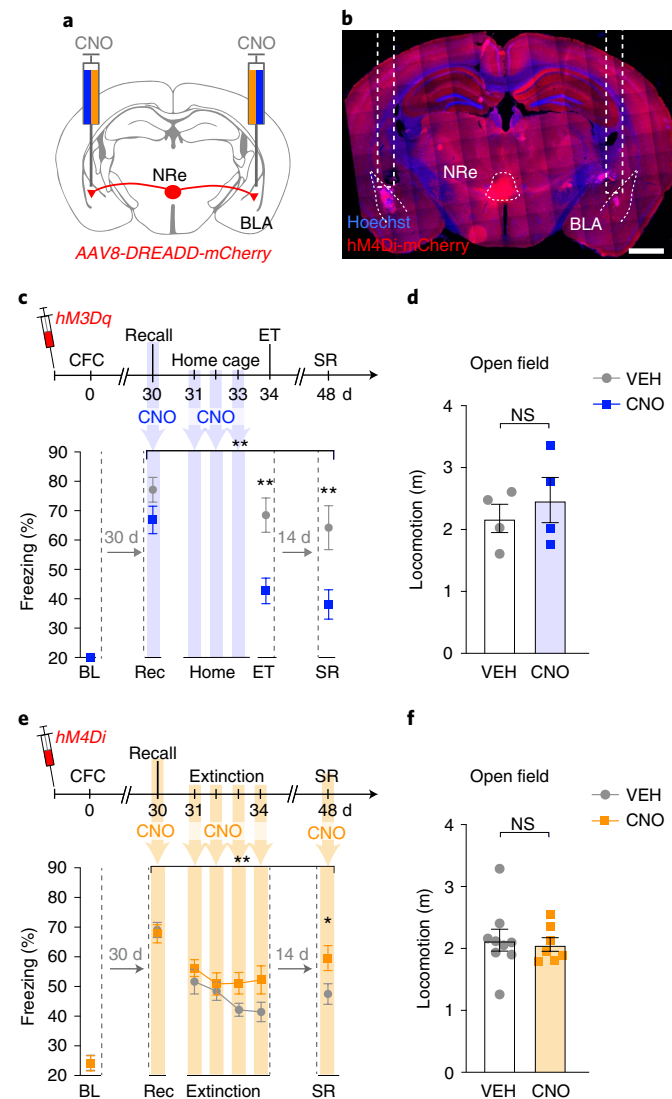
**Fig. 6 | NRe projections to the BLA are potentiated upon remote fear memory extinction.** **a**, Top: schematic of the experimental setup for ex vivo patch-clamp recordings in NRe→BLA pyramidal cells; bottom: representative picture of *Chronos-Tom*<sup>+</sup> NRe→BLA fibers. Scale bar, 250 μm. **b**, Schematic representation of the experimental groups for ex vivo patch-clamp recordings. **c**, Left: representative traces of EPSCs elicited by LED pulses in BLA pyramidal cells from mice derived from groups in **b**. Inward currents are AMPA-EPSCs recorded at -70 mV, and outward currents are NMDA-EPSCs recorded at +40 mV. Right: values of AMPA/NMDA ratio. One-way ANOVA,  $F_{3,40} = 5.234$ ,  $P = 0.0038$ , Sidak's multiple comparison, \* $P < 0.05$ , \*\* $P < 0.01$ ,  $n = 8$  (CFC only), 11 (No shock), 13 (Recall) and 12 (Ext) cells recorded from 3–4 mice per behavioral group. **d**, Top: experimental timeline for ex vivo electrophysiology in mice that underwent the spaced extinction paradigm under chemogenetic inhibition of the NRe. Patch-clamp recordings were performed 1 d after in the absence of CNO/VEH treatment. Bottom: representative traces depicting AMPA- and NMDA-EPSCs in BLA pyramidal cells from mice receiving CNO/VEH during extinction. Right: AMPA/NMDA ratio from CNO/VEH-treated animals. Two-tailed *t*-test (Welch-corrected),  $P = 0.0176$ ,  $n = 9$  (CNO) and 13 (VEH) neurons per group (from 3–4 animals per group). **e**, Experimental timeline (top) and freezing responses (bottom) during a suboptimal remote fear memory extinction paradigm. Animals were co-injected with AAV8-hSyn::hM3Dq-mCherry and AAV1-hSyn::Chronos-Tom in the NRe and underwent CFC. Thirty days later, they underwent memory recall under CNO or VEH treatment and subsequently received CNO/VEH treatment in their home cage once per day for 3 d. On the following day, a subset of animals was taken for patch-clamp recordings while the remaining animals were tested for extinction memory (ET) and, 2 weeks later, for SR. Two-way repeated-measures ANOVA, VEH versus CNO,  $F_{1,13} = 11.71$ ,  $P = 0.0045$ , Sidak's multiple comparison, \* $P < 0.05$ ,  $n = 6$  (VEH) and 9 (CNO) animals per group. **f**, Left: representative traces of AMPA- and NMDA-EPSCs in BLA pyramidal cells from mice receiving CNO/VEH during the suboptimal extinction procedure. Right: AMPA/NMDA ratio from CNO/VEH-treated animals. Two-tailed *t*-test (Welch-corrected),  $P = 0.0304$ ,  $n = 14$  (VEH) and 15 (CNO) neurons per group (from three animals per group). Data are represented as mean ± s.e.m. Statistical analysis details for each figure panel are reported in Supplementary Table 1. ET, extinction test; Ext, extinction; Hab, habituation.

Fig. 5d). These findings show that an artificial repetitive induction of NRe activity, in combination with a suboptimal extinction paradigm, leads to synaptic potentiation in NRe→BLA inputs and to a facilitation of remote fear memory extinction.

**NRe→BLA projections mediate remote fear extinction.** Lastly, we investigated whether the NRe→BLA pathway is causally implicated in regulating fear memory extinction by using a gain-of-function and loss-of-function approach (Fig. 7a,b). For the former, we expressed the excitatory DREADD hM3Dq (AAV8-CamKII::hM3Dq-mCherry) in the NRe and activated NRe terminals in the BLA by repeated intra-amygdalar infusions of CNO in a suboptimal extinction paradigm identical to the one used for somatic NRe activation (Fig. 7c, upper panel). We found that mice receiving repeated CNO administration displayed improved fear extinction when re-exposed to the same context 1 d after the suboptimal extinction paradigm (Fig. 7c, lower panel), whereas their overall motor activity was not altered (Fig. 7d). Notably, such freezing decrease was maintained when testing for SR 14 d later in

the absence of CNO, indicating a persistent effect of NRe→BLA activation on extinction retention (Fig. 7e). Conversely, when we employed the same approach to stimulate NRe terminals in the hippocampus and the mPFC—two other NRe output areas (Extended Data Fig. 7a–c) that were previously implicated in remote fear memory extinction<sup>19</sup>—we observed no differences in freezing between CNO- and vehicle-treated animals (Supplementary Fig. 7). These findings posit that the NRe conveys extinction-promoting signals via its inputs to the BLA and that a gain of function of these projections facilitates fear memory extinction.

For the latter, we chemogenetically inhibited NRe→BLA projectors by AAV8-hSyn::hM4Di-mCherry injection into the NRe and micro-infusions of CNO into the BLA before each session of the regular remote fear extinction paradigm (Fig. 7e, upper panel). We found that the repeated inhibition of NRe→BLA neurons during the extinction paradigm impaired remote fear extinction (Fig. 7e, lower panel), without altering locomotor activity (Fig. 7f). Conversely, when we employed the same pathway-specific chemogenetic approach to inhibit another BLA input—namely IL→BLA



projectors, which did not show cFos activation upon remote fear memory extinction or recall (Fig. 1d and Extended Data Fig. 9a–c)—we observed no differences in remote fear extinction efficacy (Extended Data Fig. 9d,e). Taken together, these results identify NRe→BLA afferents as a critical BLA input that mediates the extinction of remote fear memories.

## Discussion

The present findings provide, to our knowledge, the first functional description of a neuronal circuit underlying remote fear memory extinction. Thereby, they address the paucity of research on this topic, which is surprising given the long-lasting nature of traumatic memories<sup>29</sup>, the increased resistance of remote fear memories to disruption<sup>30,31</sup> and the decreased efficacy of exposure therapy with memory age<sup>4,5,32</sup>.

Our findings stipulate that, similarly to memory consolidation, the brain circuits underlying fear extinction undergo a spatial shift over time. During consolidation, the neural substrates of fear memory storage have been found to reorganize, whereby memories become increasingly independent of anatomical structures subserving memory formation, such as the hippocampus, and progressively dependent on brain regions involved in long-term memory storage, such as cortical areas<sup>13,14</sup>. This indicates that the extinction of consolidated memories might similarly rely on a redistributed network, likely requiring additional players to the canonical extinction-mediating pathways of recent memories. Indeed, during remote fear memory extinction, we show that direct IL inputs to the BLA—a central pathway for recent fear extinction<sup>8,9,15,16</sup>—are not recruited (Fig. 1d and Extended Data Fig. 9d,e). Instead, we describe the engagement of an alternative input to the BLA for remote fear memory extinction, centered on the NRe.

We found that the NRe bidirectionally modulates remote fear extinction (Fig. 2) and that its activity is increased before the end of freezing epochs during remote fear memory extinction (Fig. 3). Moreover, by closed-loop optogenetic manipulations, we show that NRe activity is sufficient and necessary to regulate freezing length during extinction (Fig. 4). Of note, the increased neuronal activity within the NRe occurs during both remote fear memory recall and its extinction (Fig. 3d–i and Extended Data Fig. 8), despite their opposite behavioral states. Because even a single memory recall session can trigger extinction<sup>32</sup>, this finding suggests that the elevated NRe activity at remote recall might reflect an initial stage of extinction-induced learning. Accordingly, chemogenetic NRe activation at remote recall immediately triggers an extinction-facilitating effect (Fig. 2e), congruent with an incipient extinction process in the NRe, whereas chemogenetic inhibition has no effect on remote fear recall per se but impairs fear attenuation during later stages of the extinction paradigm (Fig. 2b). Consistent with such a role of the NRe in extinction learning rather than memory storage are previous findings that NRe inhibition during remote memory recall does not affect memory retention<sup>23</sup>. These results are also reminiscent of previous evidence showing that NRe activity is required for changing mnemonic strategies in spatial memory tasks<sup>33</sup> and for preventing aberrant fear responses after a change in context<sup>34</sup>. Nevertheless, it remains to be determined whether, during remote fear extinction training, the NRe contributes to the formation of a new memory trace of safety, referred to as ‘extinction learning’<sup>29,35</sup>, or to an updating of the original memory trace of fear<sup>36</sup>.

Downstream of the NRe, we found that remote fear memory extinction is mediated by excitatory monosynaptic projections to the BLA (Figs. 1e, 5, 6 and 7). To our knowledge, this is the first description of an extra-amygdalar BLA input, besides the well-established cortico-amygdalar projections<sup>8,9,15,16</sup>, that regulates extinction. In particular, we found that the NRe→BLA pathway is active upon freezing cessation at both remote memory recall and the end of the extinction procedure (Fig. 5b,c and Extended Data

Fig. 8), whereas this connection shows an increased AMPA/NMDA ratio only after extinction training (Fig. 6a–c). This finding suggests that, in the initial stages of extinction, the activity of NRe→BLA inputs is not sufficient to decrease freezing because of low synaptic strength but gradually induces synaptic plasticity as the extinction paradigm proceeds. Conversely, during late extinction sessions, similar NRe→BLA activity levels (Fig. 5b,c) are likely to reduce freezing because NRe→BLA synapses have undergone potentiation. In line with this interpretation, we found that preventing NRe→BLA activation during remote fear memory extinction impairs fear attenuation (Fig. 2a,b) and is accompanied by blunted synaptic plasticity (Fig. 6d), whereas artificially increasing such plasticity facilitates fear extinction (Fig. 6e,f). Because the BLA is part of an intra-amygdalar circuit implicated in extinction learning<sup>9,37</sup>, activation of NRe→BLA inputs might trigger extinction-promoting amygdalar microcircuits<sup>8,38</sup>, such as from the BLA to the CeAl<sup>37</sup> (Extended Data Fig. 7), but this remains to be experimentally investigated.

The current data cannot exclude that other BLA inputs, such as VTA→BLA projections<sup>39</sup> (Extended Data Fig. 2), might also contribute to remote fear extinction. Neither can they rule out that other NRe outputs might participate in mediating fear extinction. Of particular interest here is hippocampal area CA1 because of its postulated role in retrieval suppression<sup>40</sup>. However, our results provide an initial indication against such scenario as chemogenetic activation of the NRe→CA1 pathway neither induces cFos activity in CA1 (Extended Data Fig. 7a–c) nor affects remote fear extinction efficiency (Supplementary Fig. 7c,d).

Upstream, the NRe is likely to receive contextual information from the IL, a brain area strongly implicated in fear extinction<sup>9</sup>, whose projections to another midline thalamic nucleus, the paraventricular nucleus of the thalamus (PVT), have recently been related to extinction retrieval<sup>41</sup>. We found that IL→NRe projectors show elevated cFos activation upon remote fear memory extinction (Fig. 1f and Extended Data Fig. 10a–c) and that their optogenetic activation facilitates fear attenuation during remote extinction (Extended Data Fig. 10d,e). These results are, at first sight, reminiscent of a previous report indicating that inhibition of mPFC→NRe afferents impairs the extinction of recently acquired fear memories<sup>42,43</sup>. Nevertheless, here, by using an unbiased neuronal mapping approach, we did not find IL→NRe afferents to be activated upon recent fear memory extinction (Fig. 1i; but this might depend on the exact extinction paradigm being used). Instead, we found IL→BLA projectors, which are known to be implicated in recent fear memory extinction<sup>8,9,15,16</sup>, to be active (Fig. 1g and Extended Data Fig. 1e). Taking both findings into consideration, we hypothesize that, although the IL→NRe projection can already modulate extinction at recent time points, it becomes the predominant route upstream of the BLA for mediating extinction at remote time points (Fig. 1f and Extended Data Figs. 1e and 10d,e) when the IL→BLA pathway is no longer active (Fig. 1d and Extended Data Fig. 9a–c) nor functionally relevant (Extended Data Fig. 9d,e). Such engagement of the IL→NRe at remote time points is also underscored by in vivo fiber photometry recordings (Extended Data Fig. 10f–h). Interestingly, although the activity of the IL→NRe pathway is enhanced at extinction, it is not time-locked to freezing cessation as the pan-NRe and NRe→BLA activities are (Figs. 3 and 5a–c). Thus, the NRe is likely to integrate additional upstream information, the origins of which remain to be identified.

One possible type of information upstream to the NRe is that about internal state. Such information originates in lower-order brain structures such as the hypothalamus<sup>44</sup>, brainstem areas including the periaqueductal gray<sup>44</sup> or the VTA, from which the NRe receives dense inputs<sup>45</sup>. Moreover, NRe stimulation was recently shown to change the internal state of mice in response to perceived threats<sup>46</sup>. Accordingly, the increased NRe activity shortly before freezing cessation (Fig. 3) might reflect an internal state change,

which is supported by the closed-loop optogenetic NRe manipulations that directly alter freezing behavior (Fig. 4).

Lastly, our findings contribute to paint a more general picture for the implication of midline thalamic nuclei in remote fear memory processing. On the one hand, the interplay between prefrontal cortical regions and midline thalamic nuclei<sup>47</sup>, including the NRe<sup>22,23,48</sup> and the PVT<sup>49</sup>, was recently found relevant for remote fear memory storage. On the other hand, here, we identify the NRe to route fear-related information from the IL to the BLA for remote fear memory extinction. Thus, in addition to the well-established direct cortico-amygdalar pathway underlying recent fear memory retrieval and extinction<sup>8,9,15,16</sup>, there appears to be an indirect cortico-thalamo-amygdalar route for fear memory modulation that becomes dominant after consolidation. When and how such spatiotemporal shift precisely occurs remain to be investigated. Harnessing this knowledge will undoubtedly help to further understand how traumatic memories of different ages are stored and can be attenuated.

## Online content

Any methods, additional references, Nature Research reporting summaries, source data, extended data, supplementary information, acknowledgements, peer review information; details of author contributions and competing interests; and statements of data and code availability are available at <https://doi.org/10.1038/s41593-021-00856-y>.

Received: 31 December 2019; Accepted: 15 April 2021;  
Published online: 20 May 2021

## References

1. Davidson, J. R. T., Stein, D. J., Shalev, A. Y. & Yehuda, R. Posttraumatic stress disorder: acquisition, recognition, course, and treatment. *J. Neuropsychiatry Clin. Neurosci.* **16**, 135–147 (2014).
2. Foa, E. B. & Kozak, M. J. Emotional processing of fear: exposure to corrective information. *Psychol. Bull.* **99**, 20–35 (1986).
3. Cukor, J., Olden, M., Lee, F. & Difede, J. Evidence-based treatments for PTSD, new directions, and special challenges. *Ann. N. Y. Acad. Sci.* **1208**, 82–89 (2010).
4. Costanzi, M., Cannas, S., Saraulli, D., Rossi-Arnaud, C. & Cestari, V. Extinction after retrieval: effects on the associative and nonassociative components of remote contextual fear memory. *Learn. Mem.* **18**, 508–518 (2011).
5. Gräff, J. et al. Epigenetic priming of memory updating during reconsolidation to attenuate remote fear memories. *Cell* **156**, 261–276 (2014).
6. Kearns, M. C., Ressler, K. J., Zatzick, D. & Rothbaum, B. O. Early interventions for PTSD: a review. *Depression Anxiety* **29**, 833–842 (2012).
7. Centonze, D., Siracusano, A., Calabresi, P. & Bernardi, G. Removing pathogenic memories: a neurobiology of psychotherapy. *Mol. Neurobiol.* **32**, 123–132 (2005).
8. Marek, R., Sun, Y. & Sah, P. Neural circuits for a top-down control of fear and extinction. *Psychopharmacology* **236**, 313–320 (2019).
9. Herry, C. et al. Neuronal circuits of fear extinction. *Eur. J. Neurosci.* **31**, 599–612 (2010).
10. Fullana, M. A. et al. Fear extinction in the human brain: a meta-analysis of fMRI studies in healthy participants. *Neurosci. Biobehav. Rev.* **88**, 16–25 (2018).
11. Pape, H.-C. & Pare, D. Plastic synaptic networks of the amygdala for the acquisition, expression, and extinction of conditioned fear. *Physiol. Rev.* **90**, 419–436 (2010).
12. Myers, K. M. & Davis, M. Mechanisms of fear extinction. *Mol. Psychiatry* **12**, 120–150 (2007).
13. Frankland, P. W. & Bontempi, B. The organization of recent and remote memories. *Nat. Rev. Neurosci.* **6**, 119–130 (2005).
14. Albo, Z. & Gräff, J. The mysteries of remote memory. *Philos. Trans. R. Soc. B Biol. Sci.* **373**, 1742 (2018).
15. Knapska, E. et al. Functional anatomy of neural circuits regulating fear and extinction. *Proc. Natl Acad. Sci. USA* **109**, 17093–17098 (2012).
16. Bloodgood, D. W., Sugam, J. A., Holmes, A. & Kash, T. L. Fear extinction requires infralimbic cortex projections to the basolateral amygdala. *Transl. Psychiatry* **8**, 60 (2018).
17. Gale, G. D. et al. Role of the basolateral amygdala in the storage of fear memories across the adult lifetime of rats. *J. Neurosci.* **24**, 3810–3815 (2004).
18. Kitamura, T. et al. Engrams and circuits crucial for systems consolidation of a memory. *Science* **356**, 73–78 (2017).

19. Silva, B. A., Burns, A. M. & Gräff, J. A cFos activation map of remote fear memory attenuation. *Psychopharmacology* **236**, 369–381 (2018).
20. Khalaf, O. et al. Reactivation of recall-induced neurons contributes to remote fear memory attenuation. *Science* **360**, 1239–1242 (2018).
21. Tervo, D. G. R. et al. A designer AAV variant permits efficient retrograde access to projection. *Neurons Neuron* **92**, 372–382 (2016).
22. Vetere, G. et al. Chemogenetic interrogation of a brain-wide fear memory network in mice. *Neuron* **94**, 363–374 (2017).
23. Sierra, R. O. et al. Reconsolidation-induced rescue of a remote fear memory blocked by an early cortical inhibition: involvement of the anterior cingulate cortex and the mediation by the thalamic nucleus reuniens. *Hippocampus* **27**, 596–607 (2017).
24. Troyner, F., Bicca, M. A. & Bertoglio, L. J. Nucleus reuniens of the thalamus controls fear memory intensity, specificity and long-term maintenance during consolidation. *Hippocampus* **28**, 602–616 (2018).
25. Schwarz, L. A. et al. Viral-genetic tracing of the input–output organization of a central noradrenaline circuit. *Nature* **524**, 88–92 (2015).
26. Barnett, L. M., Hughes, T. E. & Drobizhev, M. Deciphering the molecular mechanism responsible for GCaMP6m’s Ca<sup>2+</sup>-dependent change in fluorescence. *PLoS ONE* **12**, e0170934 (2017).
27. Vertes, R. P., Hoover, W. B., Do Valle, A. C., Sherman, A. & Rodriguez, J. J. Efferent projections of reuniens and rhomboid nuclei of the thalamus in the rat. *J. Comp. Neurol.* **499**, 768–796 (2006).
28. Kim, W. Bin & Cho, J. H. Encoding of discriminative fear memory by input-specific LTP in the amygdala. *Neuron* **95**, 1129–1146 (2017).
29. *Diagnostic and Statistical Manual of Mental Disorders, Fifth Edition* (American Psychiatric Association, 2013).
30. Milekic, M. H. & Alberini, C. M. Temporally graded requirement for protein synthesis following memory reactivation. *Neuron* **36**, 521–525 (2002).
31. Frankland, P. W. et al. Stability of recent and remote contextual fear memory. *Learn. Mem.* **13**, 451–457 (2006).
32. An, X., Yang, P., Chen, S., Zhang, F. & Yu, D. An additional prior retrieval alters the effects of a retrieval-extinction procedure on recent and remote fear memory. *Front. Behav. Neurosci.* **11**, 259 (2018).
33. Cholvin, T. et al. The ventral midline thalamus contributes to strategy shifting in a memory task requiring both prefrontal cortical and hippocampal functions. *J. Neurosci.* **33**, 8772–8783 (2013).
34. Xu, W. & Südhof, T. C. A neural circuit for memory specificity and generalization. *Science* **339**, 1290–1295 (2013).
35. Quirk, G. J. & Mueller, D. Neural mechanisms of extinction learning and retrieval. *Neuropsychopharmacology* **33**, 56–72 (2008).
36. Troyner, F. & Bertoglio, L. J. Nucleus reuniens of the thalamus controls fear memory reconsolidation. *Neurobiol. Learn. Mem.* **177**, 107343 (2021).
37. Ehrlich, I. et al. Amygdala inhibitory circuits and the control of fear memory. *Neuron* **62**, 757–771 (2009).
38. Likhtik, E., Popa, D., Apergis-Schoute, J., Fidacaro, G. A. & Paré, D. Amygdala intercalated neurons are required for expression of fear extinction. *Nature* **454**, 642–645 (2008).
39. Salinas-Hernández, X. I. et al. Dopamine neurons drive fear extinction learning by signaling the omission of expected aversive outcomes. *eLife* **7**, e38818 (2018).
40. Anderson, M. C., Bunce, J. G. & Barbas, H. Prefrontal–hippocampal pathways underlying inhibitory control over memory. *Neurobiol. Learn. Mem.* **134**, 145–161 (2016).
41. Tao, Y. et al. Projections from infralimbic cortex to paraventricular thalamus mediate fear extinction retrieval. *Neurosci. Bull.* **37**, 229–241 (2020).
42. Ramanathan, K. R., Jin, J., Giustino, T. F., Payne, M. R. & Maren, S. Prefrontal projections to the thalamic nucleus reuniens mediate fear extinction. *Nat. Commun.* **9**, 4527 (2018).
43. Ramanathan, K. R. & Maren, S. Nucleus reuniens mediates the extinction of contextual fear conditioning. *Behav. Brain Res.* **374**, 112114 (2019).
44. Silva, B. A., Gross, C. T. & Gräff, J. The neural circuits of innate fear: detection, integration, action, and memorization. *Learn. Mem.* **23**, 544–555 (2016).
45. McKenna, J. T. & Vertes, R. P. Afferent projections to nucleus reuniens of the thalamus. *J. Comp. Neurol.* **480**, 115–142 (2004).
46. Salay, L. D., Ishiko, N. & Huberman, A. D. A midline thalamic circuit determines reactions to visual threat. *Nature* **557**, 183–189 (2018).
47. DeNardo, L. A. et al. Temporal evolution of cortical ensembles promoting remote memory retrieval. *Nat. Neurosci.* **22**, 460–469 (2019).
48. Wheeler, A. L. et al. Identification of a functional connectome for long-term fear memory in mice. *PLoS Comput. Biol.* **9**, e1002853 (2013).
49. Do-Monte, F. H., Quinones-Laracuente, K. & Quirk, G. J. A temporal shift in the circuits mediating retrieval of fear memory. *Nature* **519**, 460–463 (2015).

**Publisher's note** Springer Nature remains neutral with regard to jurisdictional claims in published maps and institutional affiliations.

© The Author(s), under exclusive licence to Springer Nature America, Inc. 2021

## Methods

**Animals.** Animals used were C57BL/6JRj male mice obtained from Janvier Labs. Animals were delivered at 5–7 weeks of age and allowed an acclimatization period of 1 week before testing. Animals between 8 and 13 weeks of age were used for behavioral experiments. All animals were housed at 22–25 °C/55% humidity on a 12-h light/dark cycle (light on 7:00) with water and food ad libitum. Mice were housed in groups of four animals except for cFos analysis experiments, where animals were single housed 2 d before sacrifice. All animals were handled according to protocols and ethical guidelines approved by Swiss animal licenses VD2808 and VD2808.1, approved by the federal Food Safety and Veterinary Office of the Federal Council of Switzerland. Data collection was randomized, and data collection was performed by an experimenter blinded to the experimental conditions.

**NRe identification.** Owing to their homogeneity and small size, thalamic nuclei are often defined by vague anatomical criteria. Nonetheless, mouse brain atlases<sup>50,51</sup> indicate a division of the ventral portion of the midline thalamus (NRe) into several sub-nuclei, including the nucleus reunions (Re) medial xiphoid (Xi) and paraviphipoid (PaXi), the perireunions nucleus (PR) or ventral reunions nucleus (VRe) and the rhomboid nucleus (Rh). Owing to their small size and close proximity, it is nearly impossible to distinguish between the NRe sub-nuclei when performing local injections or lesions. Here we refer to ‘NRe’ as the combination of Re, Xi and PaXi, as described elsewhere<sup>51</sup>. For cFos and retrograde studies, photometry and optogenetics NRe borders were very clearly defined, whereas, for chemogenetic manipulations, some virus spillover in other ventral midline thalamic nuclei, including the PR and Rh, could not be avoided.

**Behavioral testing.** CFC consisted of a 3-min habituation to the conditioning chamber (TSE Systems) followed by three 2-s foot shocks (0.8 mA) with an interval of 28 s. After the shocks, animals were kept in the conditioning chamber for an additional 15 s. One day (recent) or 4 weeks (remote) later, mice were re-exposed to the same chamber for 3 min without receiving the foot shock (‘Recall’) and returned to their home cage. On the following day, they underwent a spaced extinction protocol, for which they were re-exposed to the same context two times for 3 min each, separated by a 1-h inter-trial interval, during which they were returned to their home cage. The same procedure was repeated for 4 d. Two weeks later, the SR of the extinguished memory was assessed by testing freezing during a 3-min exposure to the conditioning context. Animals belonging to the ‘No shock’ groups (Figs. 1 and 6, Extended Data Figs. 1, 2, 8, 9 and 10 and Supplementary Fig. 5) underwent the same procedure but did not receive the foot shocks. For DREADD manipulation experiments<sup>52</sup>, virus injection surgery was performed 1 week before (Fig. 6d, Extended Data Figs. 4a and 9 and Supplementary Fig. 7) or 1 week after (Figs. 2 and 6e,m, Extended Data Figs. 4b,d and 5c and Supplementary Fig. 6) fear conditioning, and CNO (Sigma-Aldrich, 3 mg kg<sup>-1</sup>) or vehicle was injected intraperitoneally 30 min before behavioral testing. For local CNO infusion experiments (Fig. 7, Extended Data Fig. 9 and Supplementary Fig. 7), virus injection surgery was performed 2 weeks before fear conditioning, and cannula implantation surgery was performed 5 weeks later. Ten minutes before behavioral testing, 150 nl of vehicle (0.9% NaCl, B. Braun) or CNO (150 μM) was injected bilaterally with an automatic pump (flow, 0.07 μl min<sup>-1</sup>). For all DREADD/CNO experiments, CNO was dissolved in sterile 0.9% NaCl (B. Braun), which was administered as vehicle.

All behavioral testing was performed between 8:00 and 12:00, and animals were randomly assigned to the different experimental groups. Percentage of time spent freezing over total context exposure time was automatically calculated with an infrared beam detection system (Multi Conditioning System, TSE Systems). Freezing was quantified when absence of movement was detected for more than 0.5 s. Open field testing was performed in a circular arena where mice were left for 10 min to freely explore, 30 min after vehicle or CNO intraperitoneal injections or 10 min after CNO micro-infusion into the BLA. Video tracking and quantification of locomotion in the open field were performed with the EthoVision tracking system.

**Fiber photometry.** Experiments were performed with a one-site, two-color fiber photometry system (Doric Lenses) measuring both the 405-nm isosbestic and the 465-nm calcium-dependent GCaMP6f fluorescence on a single photodetector<sup>53</sup>. Signals were recorded at 12 kHz using the built-in lock-in mode (Doric Neuroscience Studio). Briefly, 405-nm and 465-nm fiber-coupled LEDs were sinusoidally modulated at 531 Hz and 211 Hz, respectively, passed through an excitation filter and focused into a 400-μm fiber (NA 0.48) coupled to the mouse optic fiber implant. Emitted light was collected through the same fiber, passed through an emission filter and detected by a photoreceiver module (Newport, 2151). The LED power was kept constant for every animal and every experimental session. Behavioral data from the TSE fear conditioning system were synchronized to the fluorescence data using a transistor-transistor logic pulse at the start and end of each session. Animals were habituated to the patch cord once a day for 5 d before the beginning of the behavioral experiment. At the start of each behavioral session, animals were connected to the patch cord in a neutral familiar housing cage, and baseline GCaMP6f signals were recorded for 3 min. Immediately thereafter, animals were gently transferred to the fear conditioning boxes for behavioral testing. Acquired data files were processed with custom-written codes

in R (v3.5.0)<sup>54</sup> and Igor Pro 8 (WaveMetrics). Photometry traces were binned every 10 ms and aligned to freezing data generated by the TSE automatic infrared beam break-based scoring. Photometry traces were then low-pass filtered at 1.7 Hz using a Hanning filter (2.5 rejection band), and 405-nm and 465-nm fluorescence signals were normalized within each session by calculating  $dF/F$  as  $(F\text{-median}(F_{\text{bas}}))/\text{median}(F_{\text{bas}})$ , where  $\text{median}(F_{\text{bas}})$  was calculated over the 3-min baseline. Before further data analysis, data were screened for recording stability using the 405-nm signal, and animals were excluded from the analysis in case of loose fiber coupling, which resulted in large fluctuations in both signals.

To analyze traces at the end of freezing bouts, epochs of ±2 s around the end of each freezing event were extracted (named hereafter  $(dF/F)_{\text{FreeEnd}}$ ), aligned and averaged within each behavioral session, regardless of the duration of the following mobility bout. Only freezing bouts longer than 1.5 s were used for this analysis. To assess changes of photometry signals at freezing end,  $\Delta(dF/F)_{\text{FreeEnd}}$  was calculated by subtracting mean values of  $(dF/F)_{\text{FreeEnd}}$  before (between -0.6 s and -0.4 s) and after (between 0.0 s and 0.2 s) freezing end (occurring at 0.0 s). The slope of the calcium-dependent signal preceding freezing end was calculated as mean of the first derivative of  $(dF/F)_{\text{FreeEnd}}$  between -0.4 s and 0.0 s. To calculate the time relative to the end of freezing of the steepest increase of  $(dF/F)_{\text{FreeEnd}}$ , we calculated the time corresponding to the maximum of the first derivative of  $(dF/F)_{\text{FreeEnd}}$ . The onset of the  $(dF/F)_{\text{FreeEnd}}$  rise was calculated as the time corresponding to the maximum of the third derivative of  $(dF/F)_{\text{FreeEnd}}$  around freezing end (from -0.8 s to 0.2 s relative to freezing end). Signal power analysis (Extended Data Fig. 10h) was calculated as the sum of squares of the  $dF/F$  for each behavioral session  $\Sigma(dF/F - \text{average}(dF/F))^2$ .

**Optogenetic experiments.** For closed-loop optogenetic experiments, 2 weeks after surgery, mice were habituated for 2 d to the patch cord (200-μm diameter and 0.22 NA, Doric Lenses, 3 min each day). On the following day, mice underwent CFC and recall 30 d later. No light was delivered during CFC and recall sessions, although mice were connected to the patch cord. On the following day, during the first extinction session, mice with fiber optic implants were connected to the patch cord delivering blue light from a 473-nm laser (optogenetic activation) or yellow light from a 593-nm laser (optogenetic inhibition). Blue light was delivered for 2 s in 10-ms pulses at 20 Hz every time one freezing epoch exceeded 1 s of duration, whereas yellow light was continuously delivered for 2 s every time one freezing epoch exceeded 1 s of duration. The light power at the fiber tip was about 10 mW. Real-time freezing behavior was automatically detected with an infrared beam detection system (MultiConditioning System). The photostimulation protocol was chosen based on previous results<sup>46</sup> showing that optogenetic stimulation of the NRe with these parameters has no unspecific effect on behavior and that 20 Hz is within the physiological range of NRe neuronal firing.

For IL→NRe optogenetic activation, 2 weeks after animals received stereotaxic viral injections and fiber implants, they underwent CFC. Thirty days later, they received one recall session without light stimulation. On the following day, animals underwent remote fear memory extinction with an intermittent light stimulation (20 Hz, 5 s light ON, 5 s light OFF, total duration = 3 min). Freezing time was calculated as the average time freezing across every light ON or light OFF epochs of the session.

**Viral injections, NMDA injections and optic fiber and cannula implantation surgeries.** For all surgical procedures, mice were deeply anesthetized by subcutaneous injection of a mixture of fentanyl (0.05 mg kg<sup>-1</sup>, Sintetica), midazolam (5 mg kg<sup>-1</sup>, Actavis) and medetomidine (0.5 mg kg<sup>-1</sup>, Orion Pharma). In addition, a solution containing lidocaine (6 mg kg<sup>-1</sup>) + bupivacaine (2.5 mg kg<sup>-1</sup>) was injected subcutaneously at the site of incision. At the end of the surgical procedure, an anesthesia reversal mix containing naloxone (1.2 mg kg<sup>-1</sup>, Swissmedic), flumazenil (0.5 mg kg<sup>-1</sup>, Actavis) and atipamezole (2.5 mg kg<sup>-1</sup>, Orion Pharma) was injected subcutaneously, and animals were kept on a heating pad for an additional 2 h and were administered paracetamol (500 mg per 250 ml per cage) in the drinking water for 5 d. All stereotaxic injections were performed using a glass pipette (intraMARK, 10–20-μm tip diameter, BLAUBRAND, injection flow: 0.1 μl min<sup>-1</sup>) connected to a syringe and a stereotaxic micromanipulator (Kopf Instruments). After injection, the capillary was left at the injection site for 5 min before slow withdrawal to allow diffusion and minimize backflow.

For BLA bilateral lesions, 300 nl of NMDA (20 μg μl<sup>-1</sup>, Sigma-Aldrich) dissolved in PBS was injected at -1.12 mm AP, ±3.28 mm ML, -4.95 mm DV (control animals were injected with the same volume of PBS).

For pan-NRe fiber photometry experiments, 300 nl of AAV8-CamKII::GCaMP6f (2.3 × 10<sup>13</sup>, UPenn) was injected at a 15° off-midline angle at -1.0 mm AP, -1.1 mm ML, -4.26 mm DV.

For NRe→BLA fiber photometry experiments, 2 × 300 nl of AAV2r-Pgk::Cre (7.2 × 10<sup>12</sup>, Addgene) was injected bilaterally in the BLA at -1.12 mm AP, ±3.28 mm ML, -4.95, and 300 nl of AAV1-hSyn::FLEX-GCaMP6f (1.9 × 10<sup>13</sup>, Addgene) was injected at a 15° off-midline angle at -1.0 mm AP, -1.1 mm ML, -4.26 mm DV. For pan-NRe and NRe→BLA photometry experiments, a 400-μm fiber (Doric Lenses) was implanted 150 μm above the NRe injection site. For IL→NRe fiber photometry experiments, 2 × 300 nl of AAV2r-Pgk::Cre (7.2 × 10<sup>12</sup>, Addgene) was injected into the NRe at -0.85 mm AP, 0 mm ML, -4.2 mm DV and

-0.95 mm AP, 0 mm ML, -4.2 mm DV; 300 nl of *AAV8-hSyn::FLEX-GCaMP6f* ( $1.9 \times 10^{13}$ , Addgene) was injected in the IL at 1.94 mm AP, 0.5 mm ML, 2.8 mm DV; and a 400- $\mu\text{m}$  fiber (Doric Lenses) was implanted 150  $\mu\text{m}$  above the IL injection site.

For pan-NRe optogenetic activation, 400 nl of a mix of *AAV1-CamKII::Cre* ( $2.8 \times 10^{13}$ , Addgene) and *AAV1-Syn-FLEX-::Chronos-GFP*<sup>55</sup> ( $2.8 \times 10^{12}$ , UNC) or *AAV1-FLEX-CAG::GFP* (virus generously provided by Ralf Schneggenburger's lab) was injected into the NRe at -0.97 mm AP, -1.1 mm ML, -4.26 mm DV. A 200- $\mu\text{m}$  fiber (0.39 NA, Thorlabs) was implanted 150  $\mu\text{m}$  above the NRe injection site. The same coordinates were used for pan-NRe optogenetic inhibition experiments. The viral vectors used for optogenetic inhibition were as follows: *AAV1-CamKII::Cre* ( $2.8 \times 10^{13}$ , Addgene) and *AAV1-CAG-FLEX-::ArchT-GFP*<sup>56</sup> ( $4 \times 10^{12}$ , UNC) or *AAV1-FLEX-CAG::GFP* (virus generously provided by Ralf Schneggenburger's lab). For NRe $\rightarrow$ BLA optogenetic activation experiments,  $2 \times 300$  nl of *AAV2r-Pgk::Cre* ( $7.2 \times 10^{12}$ , Addgene) was injected bilaterally in the BLA, and 300 nl *AAV1-Syn-FLEX-::Chronos-GFP* ( $2.8 \times 10^{12}$ , UNC) or *AAV1-FLEX-CAG::GFP* was injected at a 15° off-midline angle at -1.0 mm AP, -1.1 mm ML, -4.26 mm DV. A 200- $\mu\text{m}$  fiber (0.39 NA, Thorlabs) was implanted 150  $\mu\text{m}$  above the NRe injection site. For IL $\rightarrow$ NRe optogenetic activation experiments,  $2 \times 300$  nl of *AAV8-hSyn::Chronos-Tom* ( $4.1 \times 10^{13}$ , Addgene) or a mix of *AAV1-CamKII::Cre* ( $2.8 \times 10^{13}$ , Addgene) and *AAV8-hSynDIO::mCherry* ( $2.3 \times 10^{13}$ , Addgene) was bilaterally injected in the IL at 2.00 mm AP,  $\pm 1.6$  mm ML, -2.04 mm DV at a 30° off-midline angle.

For DREADD experiments,  $2 \times 300$  nl of *AAV8-hSyn::hM4Di-mCherry* ( $7.4 \times 10^{12}$ , UNC) or *AAV8-CamKII::hM3Dq-mCherry* ( $9.7 \times 10^{12}$ , produced at the Bertarelli Foundation Gene Therapy Core Facility with a pAAV-CaMKIIa-hM3D(Gq)-mCherry gift from Bryan Roth, Addgene plasmid no. 50476) was injected into the NRe at -0.85 mm AP, 0 mm ML, -4.2 mm DV and -0.95 mm AP, 0 mm ML, -4.2 mm DV. When controlling for CNO unspecific effects (Extended Data Fig. 4a), we injected *AAV8-hSyn::hM4Di-mCherry* ( $7.4 \times 10^{12}$ , UNC) or a mix of *AAV1-CamKII::Cre* ( $2.8 \times 10^{13}$ , Addgene) and *AAV8-hSynDIO::mCherry* ( $2.3 \times 10^{13}$ , Addgene). The same coordinates were used to inject *AAV1-hSyn::Chronos-tdTom* ( $4.1 \times 10^{13}$ ; pAAV-Syn-Chronos-tdTomato was a gift from Edward Boyden, Addgene viral prep no. 62726-AAV1) for patch-clamp recordings.

For patch-clamp recordings, after chemogenetic manipulations of the NRe (Fig. 6d–f), the same virus was mixed with *AAV8-CamKII::hM4Di-mCherry* ( $2.6 \times 10^{13}$ , Addgene) or *AAV8-CamKII::hM3Dq-mCherry* ( $1.8 \times 10^{12}$ , VVF). For AAV2r retrograde tracing,  $2 \times 300$  nl of *AAV2r-CAG::Tom* ( $7.2 \times 10^{12}$ ; pAAV-CAG-tdTomato (codon diversified) was a gift from Edward Boyden, Addgene viral prep no. 59462-AAVrg) or *AAV2r-CAG::GFP* ( $7 \times 10^{12}$ ; pAAV-CAG-GFP was a gift from Edward Boyden, Addgene viral prep no. 37825-AAVrg) was injected into the NRe at -0.85 mm AP, 0 mm ML, -4.2 mm DV and -0.95 mm AP, 0 mm ML, -4.2 mm DV and bilaterally into the BLA at -1.12 mm AP,  $\pm 3.28$  mm ML, -4.95 mm DV.

For chemogenetic projection manipulation experiments, surgical implant of cannula guides into target sites was conducted 3 weeks after viral injections. For NRe $\rightarrow$ BLA terminal manipulation, a 4-mm cannula guide (C315G/Spc) was implanted bilaterally at -1.5 mm AP,  $\pm 2.95$  mm ML, -4.2 DV. For NRe $\rightarrow$ dCA1, a 1-mm cannula guide was implanted at -2.0 mm AP,  $\pm 1.5$  mm ML, -1.0 DV. For NRe $\rightarrow$ mPFC terminal stimulation experiments, a 4-mm cannula guide was implanted bilaterally with at 30° off-midline angle at 1.94 mm AP, -1.85 mm ML, -1.2 mm DV. For IL $\rightarrow$ BLA terminal inhibition experiments,  $4 \times 300$  nl of *AAV8-CamKII::hM4Di-mCherry* ( $2.6 \times 10^{13}$ , Addgene) was bilaterally injected in the IL at 2.03 mm AP,  $\pm 1.6$  mm ML, -2.44 mm DV and 2.13 mm AP,  $\pm 1.6$  mm ML, -2.44 mm DV at a 30° off-midline angle. A 4-mm cannula guide (C315G/Spc) was implanted bilaterally at -1.5 mm AP,  $\pm 2.95$  mm ML, -4.2 DV. After 1 week of recovery, animals were habituated to non-protruding injectors once a day for 3 d. Local infusions of CNO and vehicle were performed with a 1-mm protruding injector 10 min before behavioral testing.

For TRIO experiments,  $2 \times 300$  nl of *AAV2r-pgk::Cre* ( $7.2 \times 10^{12}$ , Addgene) was injected bilaterally in the BLA, and  $2 \times 400$  nl of a mix of *AAV1-CAG-FLEX-RabiesG-GFP* and *AAV1-CAG-FLEX-TVA* (produced at the Bertarelli Foundation Gene Therapy Core Facility) was injected into the NRe at -0.85 mm AP, 0 mm ML, -4.2 mm DV and -0.95 mm AP, 0 mm ML, -4.2 mm DV. Three weeks later,  $4 \times 300$  nl of an EnvA pseudotyped rabies virus, in which the protein G was replaced by m-Cherry (*SAD $\Delta$ G-mCherry(EnvA)*, Salk Institute Vector Core), was injected into the NRe at -0.82 mm AP, 0 mm ML, -4.2 mm DV; at -0.85 mm AP,  $\pm 0.1$  mm M/L, -4.2 mm DV; and at -0.95 mm AP, 0 mm ML, -4.2 mm DV; and mice were sacrificed 8 d later. Control animals did not receive *AAV1-CAG-FLEX-RabiesG-GFP* injection.

Representative images of anatomical locations for viral injections and optic fiber and cannula placements are shown with the corresponding experimental data or in Supplementary Fig. 8.

**Electrophysiological recordings.** Mice were deeply anaesthetized with isoflurane and decapitated. The brain was quickly removed, and 250- $\mu\text{m}$ -thick coronal slices containing the amygdala were prepared using a vibrating tissue slicer (Campden Instruments) in oxygenated (95% O<sub>2</sub>/5% CO<sub>2</sub>) ice-cold modified artificial cerebrospinal fluid (ACSF), containing (in mM): 105 sucrose, 65 NaCl, 25

NaHCO<sub>3</sub>, 2.5 KCl, 1.25 NaH<sub>2</sub>PO<sub>4</sub>, 7 MgCl<sub>2</sub>, 0.5 CaCl<sub>2</sub>, 25 glucose, 1.7 L<sup>+</sup> ascorbic acid. After cutting, slices recovered for 1 h at 35 °C in standard ACSF containing (in mM): 125 NaCl, 25 NaHCO<sub>3</sub>, 2.5 KCl, 1.25 NaH<sub>2</sub>PO<sub>4</sub>, 1.2 MgCl<sub>2</sub>, 2 CaCl<sub>2</sub>, 18 glucose, 1.7 L<sup>+</sup> ascorbic acid and complemented with 2 sodium pyruvate and 3 myo-inositol. For current-clamp recordings with somatic optogenetic stimulation, slices containing the ventromedial thalamus were superfused with oxygenated standard ACSF at nearly physiological temperature (30–32 °C). *AAV1-hSyn::Chronos-Tom*-infected NRe cells were patched in the whole-cell configuration with borosilicate glass pipettes (TW150F-3, WPI) pulled with a DMZ-Zeitz puller (Zeitz Instruments). Pipettes (3–4 M $\Omega$ ) were filled with (in mM): 130 K-gluconate, 10 KCl, 10 HEPES, 10 phosphocreatine, 0.2 EGTA, 4 Mg-ATP, 0.2 Na-GTP (290–300 mOsm, pH 7.2–7.3). NRe cell spiking was elicited by trains of 5-ms-long whole-field LED flashes (470-nm, CoolLED, 40 mW at objective exit) controlled via a Master-9 Pulse Stimulator (A.M.P. Instruments). Reliability of photoactivation in eliciting cell spiking was tested using train stimulations at 5, 10 and 20 Hz. Spiking efficiency was calculated as percentage of LED flashes eliciting at least one action potential. For voltage-clamp recordings with synaptic stimulation, slices containing the amygdala were superfused with ACSF at room temperature containing the GABA<sub>A</sub>R blocker picrotoxin (0.1 mM). Neurons identified with video-microscopy in the amygdala subnuclei were patched in the whole-cell configuration with borosilicate glass pipettes (TW150F-3, WPI) pulled with a DMZ-Zeitz puller (Zeitz Instruments). Pipettes (2–4 M $\Omega$ ) were filled with (in mM): 120 Cs-gluconate, 10 CsCl, 10 HEPES, 10 phosphocreatine, 5 EGTA, 4 Mg-ATP, 0.2 Na-GTP, 2.5 QX-314-Cl<sup>-</sup> (290–300 mOsm, pH 7.2–7.3). Visually identified neurons in the CeA and pyramidal cells in the lateral amygdala (LA) and BLA displayed membrane capacitance values that were consistent with their cell size (CeA:  $110 \pm 14$  pF,  $n = 11$ ; LA:  $173 \pm 23$  pF,  $n = 10$ ; BA:  $214 \pm 6$  pF,  $n = 6$ ). BLA neurons that displayed a capacitance <130 pF (on average  $105 \pm 9$  pF,  $n = 20$ ) were considered putative interneurons and excluded from the analysis. Thalamic afferents were photostimulated every 15 s with brief (1-ms) whole-field LED flashes (470-nm, CoolLED) controlled via a Master-9 Pulse Stimulator.

For comparison of synaptic currents between different post-synaptic targets, the maximal LED power was applied (40 mW at objective exit). For paired-pulse ratio, AMPAR-mediated EPSCs (AMPAR-EPSCs) were elicited at -70 mV by two consecutive photostimulations (50-ms interval), and the amplitude of the second response was divided by the amplitude of the first response. For AMPA/NMDA ratios, after recording AMPAR-EPSCs at -70 mV, the membrane potential was slowly switched to +40 mV, and DNQX (0.01 mM) was added to the perfuse to isolate the NMDA-EPSCs. In a subgroup of recordings, we verified that EPSCs elicited at +40 mV were blocked by the NMDAR antagonist D,L-APV (0.1 mM), which led to a current reduction of  $95.8 \pm 0.3\%$  ( $n = 23$ ). Peak values of AMPA-EPSCs were divided by the amplitude of NMDA-EPSCs, measured as the mean of 3 ms around the absolute peak. Series resistance ( $R_s$ ) and input resistance ( $R_i$ ) were monitored throughout recordings by brief voltage pulses, and data were rejected for changes in resistance >20%. Membrane voltage values were not corrected for liquid junction potential. Data were acquired through a Digidata 1550A digitizer. Signals were amplified through a MultiClamp 700B amplifier (Molecular Devices), sampled at 20 kHz and filtered at 10 kHz using Clampex 10 (Molecular Devices). Clampfit 10 (Molecular Devices) and Igor Pro 6 (WaveMetrics) were used for data analysis.

**Histology.** For all histological analyses, mice were deeply anesthetized with pentobarbital (150 mg kg<sup>-1</sup> intraperitoneally, Streuli Pharma) and perfused transcardially (4.0% paraformaldehyde, 1× PBS, pH 7.4). Brains were removed, post-fixed (4% paraformaldehyde overnight), cryoprotected (30% sucrose, 1× PBS, 4 °C, 48 h) and frozen at -80 °C, and 40- $\mu\text{m}$  coronal sections were cut with a sliding cryostat (Leica Microsystems). For cFos IHC, mice were sacrificed 90 min after behavioral testing. For cFos IHC upon hM3Dq-mediated activation, CNO injection was performed 1 week after behavioral testing, and animals were sacrificed 120 min after CNO or vehicle injection. Free-floating sections were incubated in blocking solution (1% BSA, 1× PBS, 0.3% Triton X-100, Sigma-Aldrich) at room temperature for 1 h, followed by incubation with rabbit anti-cFos antibody (1:5,000, Synaptic Systems, no. 226 003) in blocking buffer (1% BSA, 1× PBS, 0.1% Triton X-100) overnight at 4 °C under constant shaking. Sections were washed extensively with PBS/Triton 0.1% and then exposed to secondary antibody (Alexa Fluor 647-conjugated donkey anti-rabbit IgG, Life Technologies) in blocking buffer at room temperature for 2 h. They were incubated with Hoechst (Life Technologies) at 1:1,000 in PBS at room temperature for 5 min, washed extensively with PBS and mounted on Superfrost glass slides (Thermo Fisher Scientific) with Fluoromount mounting medium (SouthernBiotech). Images were acquired on a virtual slide microscope (VS120, Olympus) with an  $\times 10$  objective. For NeuN, the same IHC procedure was used (rabbit anti-NeuN antibody, 1:1,000, Merck, no. ABN78).

For verification of viral infection and cannula/fiber optic placement, one section every two sections was stained with Hoechst, mounted and imaged with a VS120  $\times 10$  microscope.

**Image analysis.** For cFos<sup>+</sup>, AAV2r<sup>+</sup>, NeuN<sup>+</sup> and Hoechst<sup>+</sup> cell detection, images were analyzed with QuPath v0.1.3 and v0.1.4 (ref. <sup>57</sup>). Briefly, brain areas were manually outlined based on the Hoechst signal following the Allen Brain Reference

Atlas, and positive cells within the outlined structures were automatically detected with the ‘positive cell detection’ built-in function. The density of cFos-positive cells ( $\text{cFos}^+$  per  $\text{mm}^2$ ) was averaged over 2–6 sections per animal. For co-localization analysis of AAV2r-, cFos- and Hoechst-positive cells, a custom-built script for QuPath was used. Chance ratios were calculated for each outlined region with the following formulas and averaged across 2–6 sections for each animal:  $(\text{double}^+/\text{Hoechst}^+)/\text{chance level}$ , where chance level was calculated as  $(\text{cFos}^+/\text{Hoechst}^+) \times (\text{AAV2r}^+/\text{Hoechst}^+)$ . Chance ratios were then normalized by ‘No shock’ controls (Fig. 1). Corresponding chance-normalized values before normalization to controls are reported in Extended Data Figs. 8, 9 and 10. Raw values of  $\text{cFos}^+/\text{Hoechst}^+$  and  $\text{AAV2r}^+/\text{Hoechst}^+$  are reported in Extended Data Fig. 1.

For anterograde tracing analysis (Supplementary Fig. 3), fiber density in the BLA and NRe was calculated as the mean mCherry or GFP intensity in the BLA or NRe normalized by background. Values were averaged across 2–6 sections per animal.

For verification of viral infection, the signal from the fluorescent reporter was manually thresholded and quantified (ImageJ). Infection efficiency (either % area or total area) was calculated over the total area of the nucleus as determined from the atlas overlay. Animals that showed less than 20% infection of the target area were excluded from the behavior analysis. Known anatomical target areas of the infected areas were carefully screened for possible off-site infection due to potential AAV transport. Optic fiber and cannula location were verified based on fiber tract lesion. AAV-Cre virus location was verified in some cases by co-injection with fluorescently labeled cholera toxin B.

**Statistics and reproducibility.** Data analysis was performed with Prism 8 software (GraphPad). All data are reported as mean  $\pm$  standard error. No statistical methods were used to predetermine sample sizes, but the number of animals used in each experiment is similar to those reported in previously published studies<sup>15,19,22,28</sup>. Data distribution was assumed to be normal, but this was not formally tested. Animals were randomly assigned to experimental groups. Animals from different experimental groups were sex and age matched. The statistical test used, definition of  $n$  and multiple hypothesis correction are described in the figure legends and Supplementary Table 1. For experiments in which animals were tested across multiple behavioral sessions, repeated-measures statistical testing was applied. Statistical analysis details for each figure are reported in Supplementary Table 1.

**Reporting Summary.** Further information on research design is available in the Nature Research Reporting Summary linked to this article.

## Data availability

All data are available from the authors upon reasonable request.

## Code availability

All code used in this manuscript is available at <https://zenodo.org/record/4588295>.

## References

50. Paxinos, G. & Franklin, K. B. J. *Paxinos and Franklin's the Mouse Brain in Stereotaxic Coordinates* (Academic Press, 2001).
51. Sunkin, S. M. et al. Allen Brain Atlas: an integrated spatio-temporal portal for exploring the central nervous system. *Nucleic Acids Res.* **41**, 996–1008 (2013).
52. Armbruster, B. N., Li, X., Pausch, M. H., Herlitze, S. & Roth, B. L. Evolving the lock to fit the key to create a family of G protein-coupled receptors potently activated by an inert ligand. *Proc. Natl Acad. Sci. USA* **104**, 5163–5168 (2007).
53. Chen, T. W. et al. Ultrasensitive fluorescent proteins for imaging neuronal activity. *Nature* **499**, 295–300 (2013).
54. R Core Team. R: A Language and Environment for Statistical Computing. <http://www.R-project.org/> (R Foundation for Statistical Computing, 2017).
55. Klaoetke, N. C. et al. Independent optical excitation of distinct neural populations. *Nat. Methods* **11**, 338–346 (2014).
56. Han, X. et al. A high-light sensitivity optical neural silencer: development and application to optogenetic control of non-human primate cortex. *Front. Syst. Neurosci.* **5**, 18 (2011).
57. Bankhead, P. et al. QuPath: open source software for digital pathology image analysis. *Sci. Rep.* **7**, 16878 (2017).

## Acknowledgements

We thank M. Curdy, F. Wyler, M. Santoboni, M. Kintscher, F. Habibollahi, C. Yildirim, R. Gros, A. Goossens, C. Benquet, D. Joly, T. Hübscher, A.-R. Warter, L. Duvaud, L. Ho Dac and N. Sato for their contributions in histological procedures, the EPFL BIOP core facility for their technical assistance with image analysis, the Bertarelli Foundation Gene Therapy Core Facility at EPFL for AAV production and L. de Lecea, S. Tyree (Stanford) and N. Banterle (EPFL) for their assistance with fiber photometry. Funding: B.A.S. is supported by an EMBO long-term fellowship (ALTI1605-2014, Marie Curie Actions, LTFCOFUND2013, GA-2013-609409). M.F.M.-R. is supported by an UNAM-DGECI International Scholarship from the National Autonomous University of Mexico (DGECI/DG/DFI/SME/1731/2016). J.G. is an MQ fellow (MQ15FPI100012) and a NARSAD Independent Investigator (24497). H.H. is supported by a NENS Exchange Grant. The laboratory of J.G. is supported by the European Research Council (ERC-2015-StG 678832), the Swiss National Science Foundation (31003 A\_155898), the National Competence Center for Research (NCCR) SYNAPSY (51NF40-185897) and the Vallee Foundation (VS-2019-27). Work from the C.S. laboratory is supported by grants from the SNSF (31003A-176206) and the NCCR SYNAPSY (158776 and 185897).

## Author contributions

This study was planned and conceptualized by B.A.S. and J.G. B.A.S. carried out the experiments and analyzed data. S.A. performed and analyzed electrophysiological experiments under the guidance of C.S. A.M.B. contributed to fiber photometry data analysis. G.S. contributed to viral injections and behavioral experiments. H.H., L.v.d.H. and M.F.M.-R. contributed to histology and image analysis. The paper was written by B.A.S. and J.G. and commented on by all authors.

## Competing interests

The authors declare no competing interests.

## Additional information

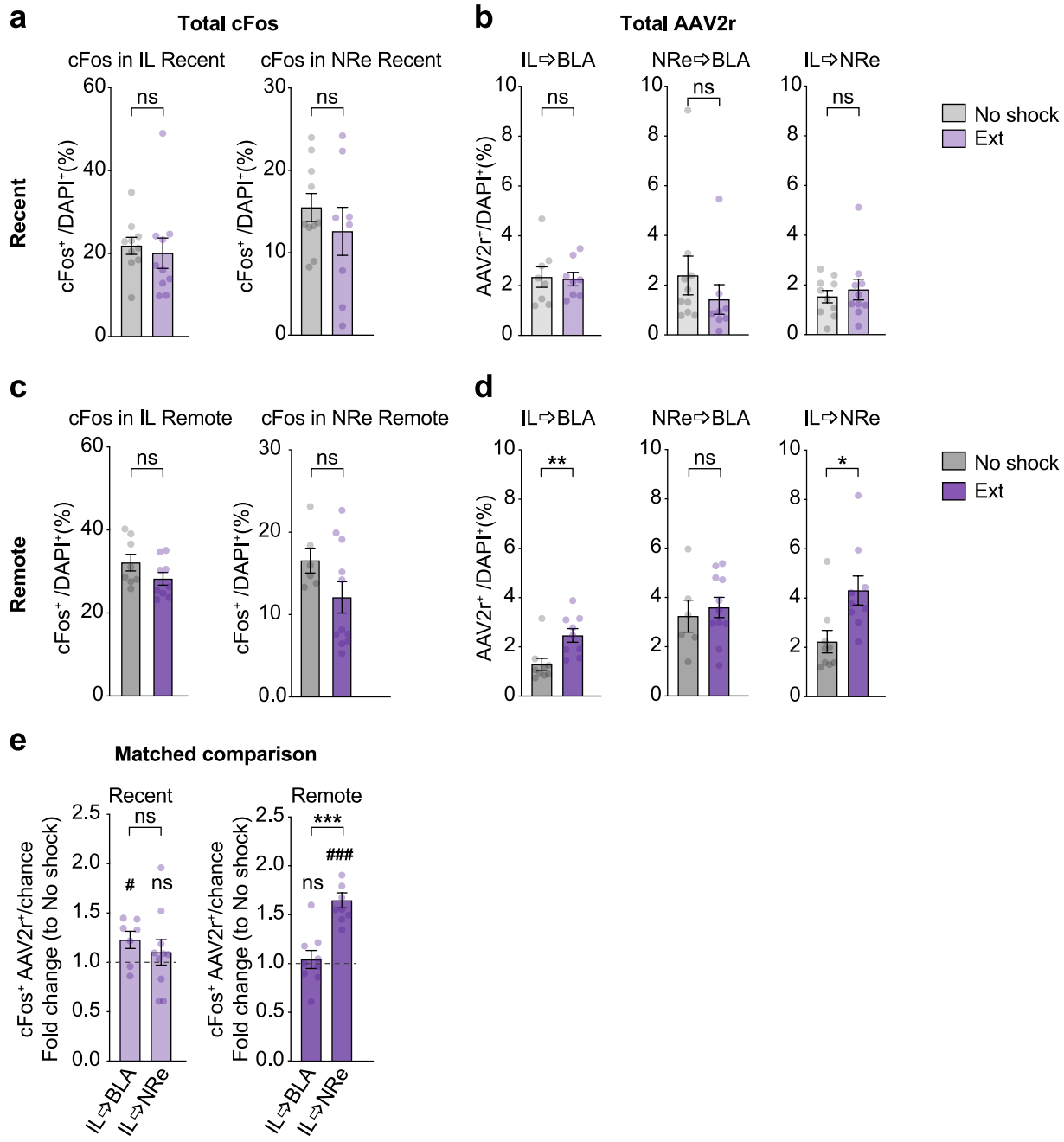
**Extended data** is available for this paper at <https://doi.org/10.1038/s41593-021-00856-y>.

**Supplementary information** The online version contains supplementary material available at <https://doi.org/10.1038/s41593-021-00856-y>.

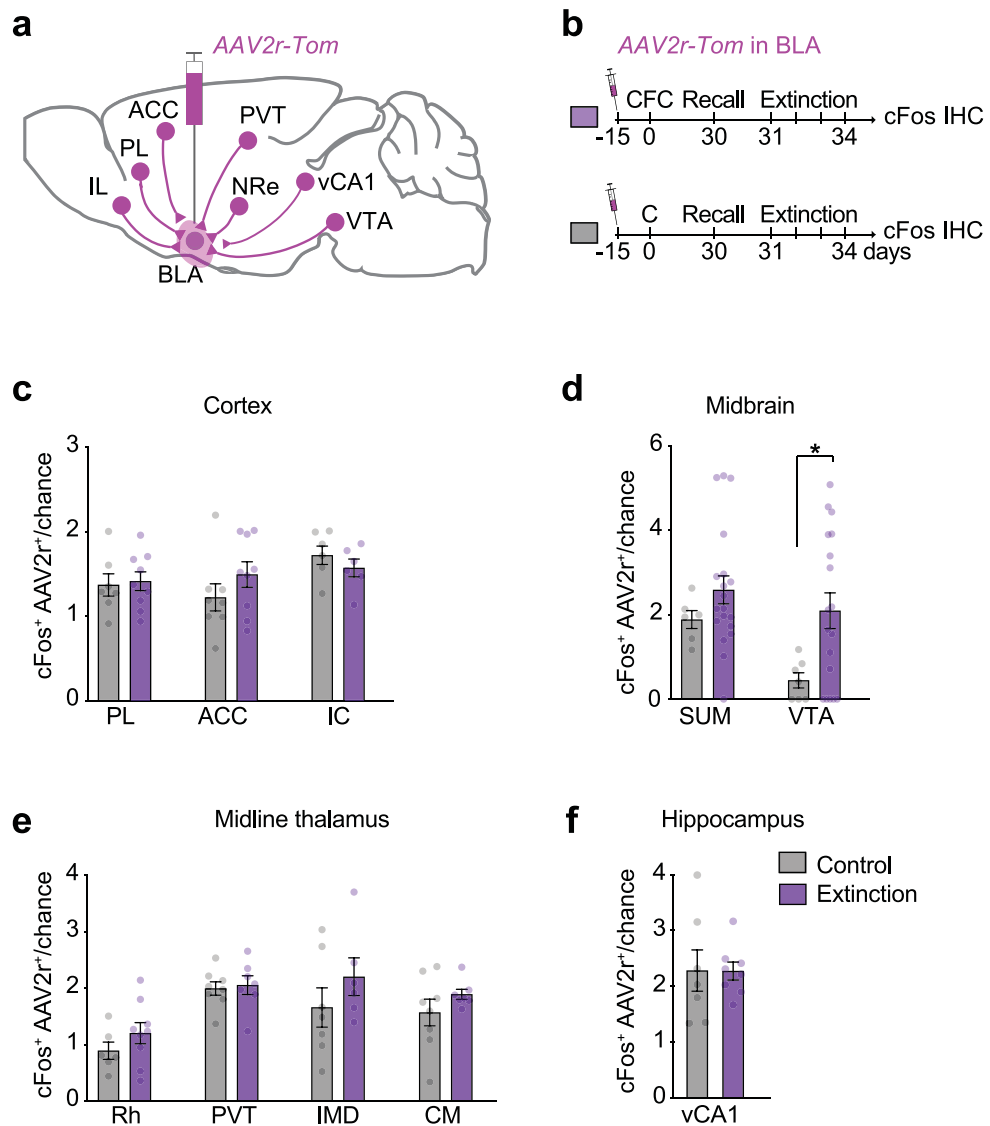
**Correspondence and requests for materials** should be addressed to J.G.

**Peer review information** *Nature Neuroscience* thanks Larry Zweifel and the other, anonymous, reviewer(s) for their contribution to the peer review of this work.

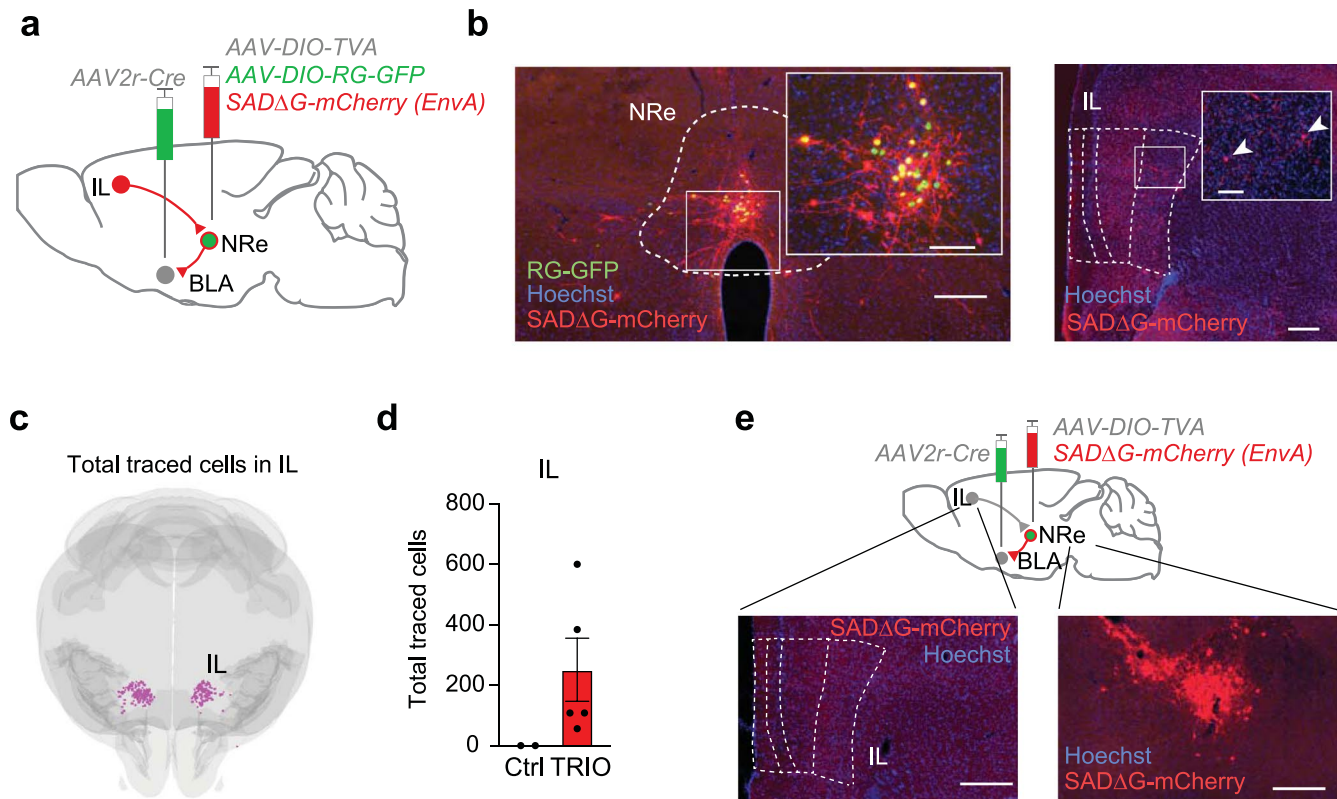
**Reprints and permissions information** is available at [www.nature.com/reprints](http://www.nature.com/reprints).



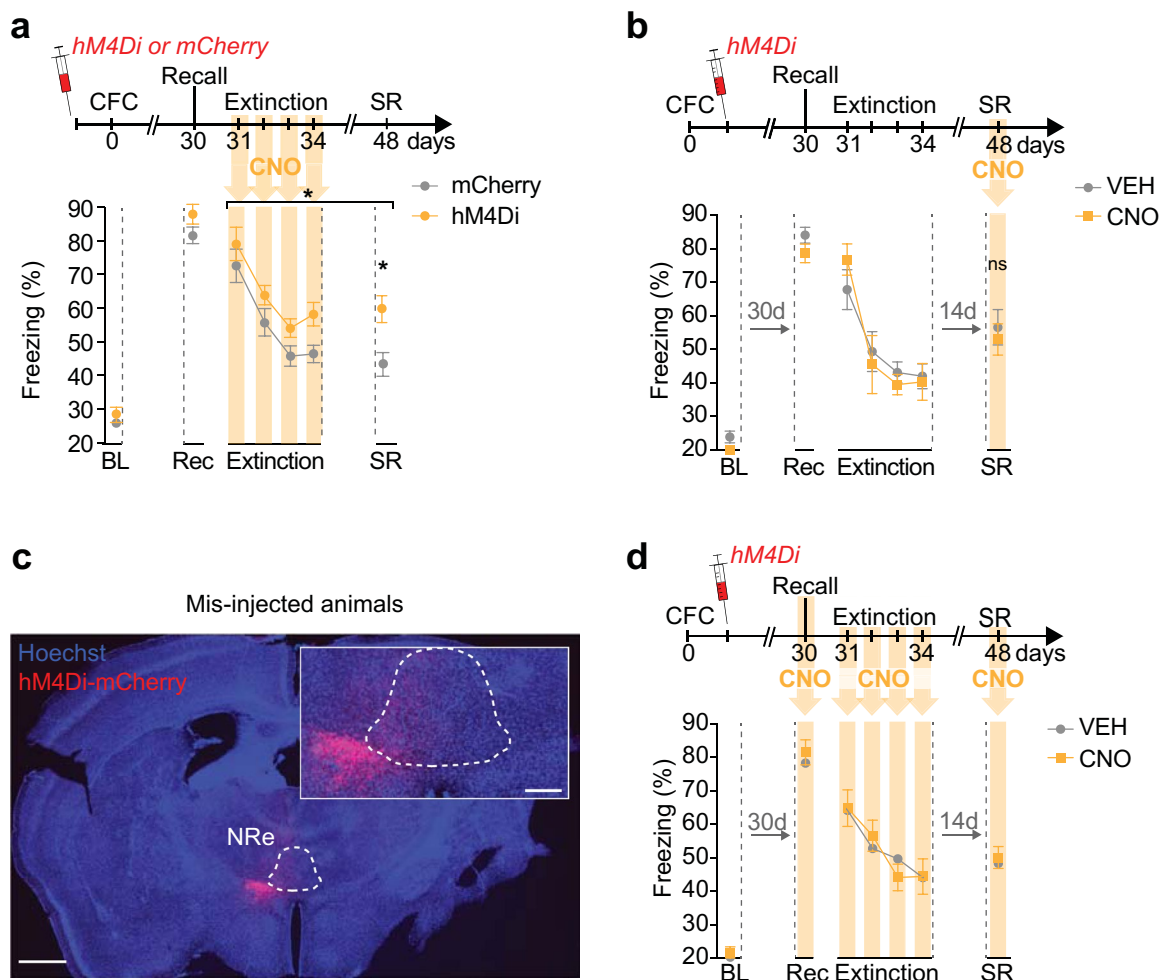
**Extended Data Fig. 1 | cFos and AAV2r quantifications in the IL, NRe and BLA upon recent and remote fear memory extinction.** **a**, Quantification of cFos<sup>+</sup> cells in the IL (left) and NRe (right) of brain sections used for functional connectivity analysis following recent fear memory extinction (Fig. 1). Unpaired t-test. IL: P = 0.6748, N = 10 mice/group; NRe: P = 0.381, N = 8 (Ext), 10 (No shock) animals/group. **b**, Quantification of AAV2r<sup>+</sup> cells in the IL and NRe of brain sections used for functional connectivity analysis following recent fear memory extinction (Fig. 1). Unpaired t-test. IL → BLA: P = 0.876, N = 8 (Ext), 8 (No shock) animals/group; NRe → BLA: P = 0.3599, N = 8 (Ext), 10 (No shock) animals/group; IL → NRe: P = 0.5688, N = 10 (Ext), 10 (No shock) animals/group. **c**, Quantification of cFos<sup>+</sup> cells in the IL (left) and NRe (right) of brain sections used for functional connectivity analysis following remote fear memory extinction (Fig. 1). Unpaired t-test. IL: P = 0.1374, N = 9 (Ext), 8 (No shock) animals/group; NRe: P = 0.1349, N = 11 (Ext), 6 (No shock) animals/group. **d**, Quantification of AAV2r<sup>+</sup> cells in the IL and NRe of brain sections used for functional connectivity analysis following remote fear memory extinction. Unpaired t-test. IL → BLA: P = 0.006, N = 9 (Ext), 8 (No shock) animals/group; NRe → BLA: P = 0.638, N = 11 (Ext), 6 (No shock) animals/group; IL → NRe: P = 0.0132, N = 9 (Ext), 9 (No shock) animals/group. **e**, Matched comparisons (within the same animals/group) of IL → BLA vs IL → NRe activation upon recent (left) or remote (right) fear memory extinction. Recent: Unpaired t-test: P = 0.1304, N = 7 animals/behavioral group. Two-tailed one-sample t-test (theoretical mean=1), IL → BLA, #P = 0.04; IL → NRe, P = 0.4476; Remote: Unpaired t-test: P = 0.0001, N = 9 animals/behavioral group. Two-tailed one-sample t-test (theoretical mean=1), IL → BLA, P = 0.6634; IL → NRe, ##P < 0.0001. BLA, basolateral amygdala; CFC, contextual fear conditioning; Ext, extinction; IL, infralimbic cortex; NRe, nucleus reuniens of the thalamus. Data are represented as mean ± SEM. Statistical analysis details for each figure panel are reported in Supplementary Table 1.



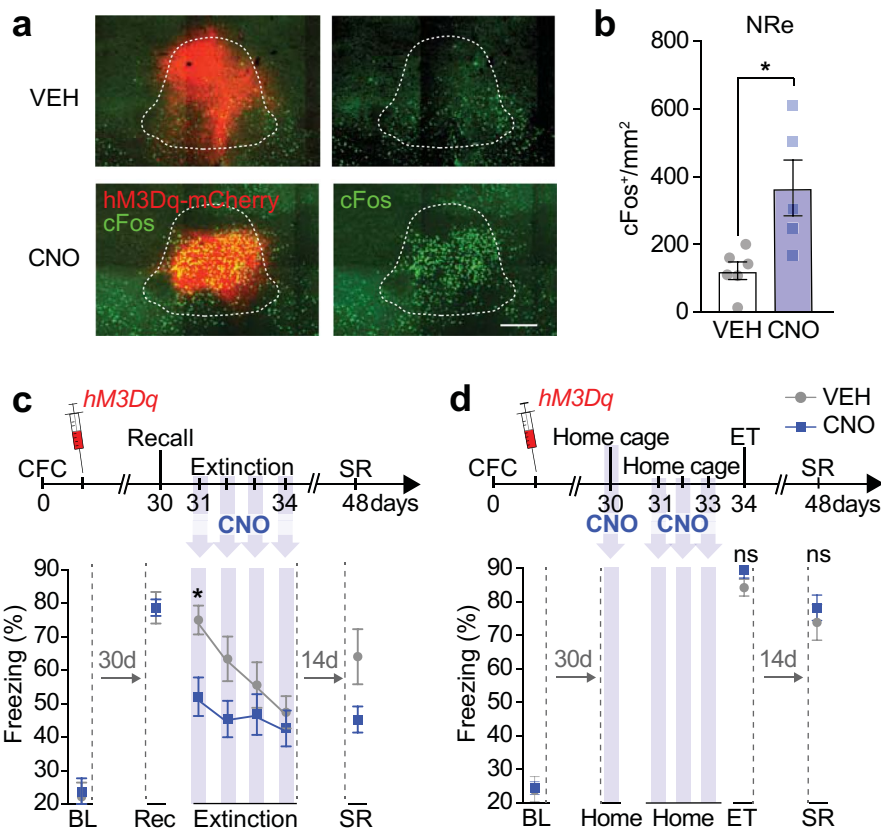
**Extended Data Fig. 2 | cFos mapping in BLA inputs.** Schematic representation of **a**, AAV2r injections into the BLA and **b**, behavioral groups used for cFos IHC in AAV2r-injected animals. Colocalization analysis of retrogradely traced cells from the BLA (AAV2r<sup>+</sup>) and cells activated upon remote fear memory recall and extinction (cFos<sup>+</sup>) in **c**, cortex: Two-way ANOVA, Control vs Extinction,  $F(1,39)=0.245$ ,  $P=0.62$ . Multiple comparison, Sidak. PL,  $N=7$  (No shock), 9 (Ext) mice/group; ACC,  $N=8$  (No shock), 9 (Ext) mice/group; IC,  $N=6$  (No shock), 6 (Ext) mice/group; **d**, midbrain: Two-way ANOVA, Control vs Extinction,  $F(1,46)=6.411$ ,  $P=0.0148$ . Multiple comparison, Sidak \*  $P < 0.05$ . SUM,  $N=6$  (No shock), 19 (Ext) mice/group; VTA,  $N=7$  (No shock), 18 (Ext) mice/group; **e**, midline thalamus: Two-way ANOVA, Control vs Extinction,  $F(1,50)=3.989$ ,  $P=0.051$ . Multiple comparison, Sidak. Rh,  $N=6$  (No shock), 9 (Ext) mice/group; PVT,  $N=8$  (No shock), 7 (Ext) mice/group; IMD  $N=7$  (No shock), 6 (Ext) mice/group; CM,  $N=8$  (No shock), 7 (Ext) mice/group. **f**, hippocampus: unpaired t test  $P=0.979$ . N = 7 (No shock), 8 (Ext) mice/group. ACC, anterior cingulate cortex; BLA, basolateral amygdala; CM, centromedial thalamus; IL, infralimbic cortex; IC, insular cortex (posterior, granular cortex); IMD, intermediodorsal nucleus of the thalamus; NRe, nucleus reuniens of the thalamus; PL, prelimbic cortex; PVT, periventricular thalamus; Rh, rhomboid nucleus; SUM, supramammillary nucleus; vCA1, ventral CA1; VTA, ventral tegmental area. Data are represented as mean  $\pm$  SEM. Statistical analysis details for each figure panel are reported in Supplementary Table 1.



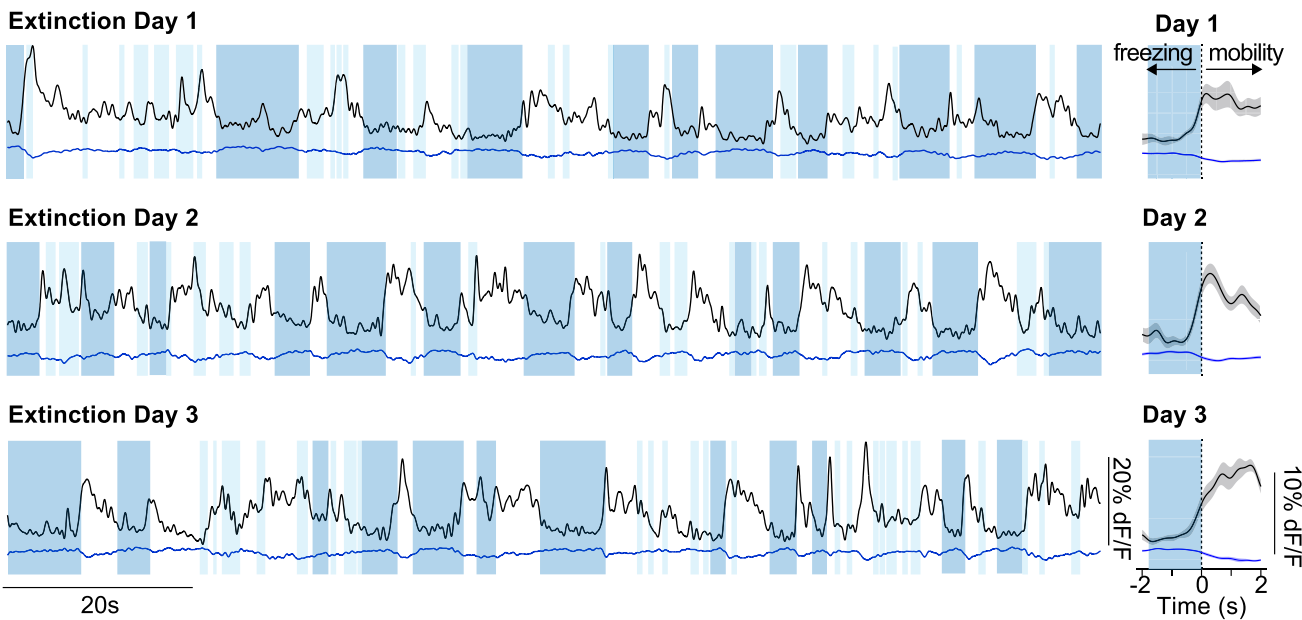
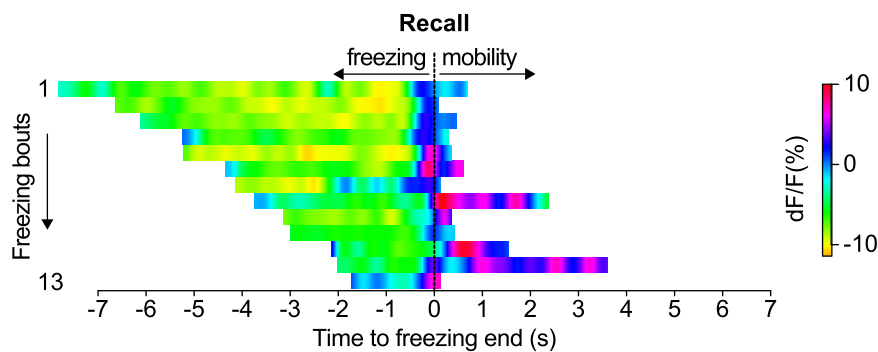
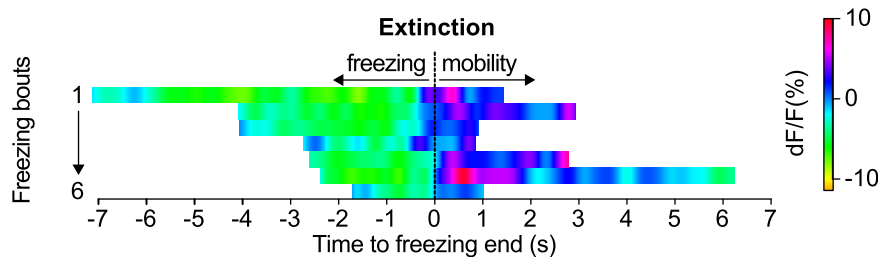
**Extended Data Fig. 3 | TRIO of a direct IL-NRe-BLA di-synaptic circuit.** (a) Schematic representation of the strategy for tracing the relationship between input and output (TRIO). An AAV2r-Cre virus was injected bilaterally into the BLA and Cre-dependent helper viruses (AAV8-DIO-TVA, AAV8-DIO-RG-GFP) were injected in the NRe. Retrograde transport of the AAV2r allows for selective expression of the Cre recombinase in NRe neurons projecting to the BLA. After Cre recombination, the helper AAVs express TVA, an avian receptor protein that confers infection capability to EnvA-pseudotyped rabies virus, and rabies glycoprotein B19G-GFP, which mediates the monosynaptic retrograde spread of rabies particles. Three weeks later, an EnvA-pseudotyped rabies virus carrying an mCherry coding sequence was injected into the NRe, which selectively infects TVA-expressing neurons and spreads retrogradely and trans-synaptically. (b) (Left) Example picture of starter cells in the NRe co-labeled with RG-GFP deriving from the Cre-dependent AAV and mCherry from the rabies virus. Scale bar = 250  $\mu$ m. Zoom-in inset: scale bar = 100  $\mu$ m. (Right) Retrogradely traced neurons in the IL identified by mCherry expression of transsynaptically transported rabies. Scale bar = 250  $\mu$ m. Zoom-in inset: scale bar = 100  $\mu$ m. Arrowheads indicate mCherry $^+$  neurons in the IL. (c) Schematic representation of mCherry $^+$  neurons in the IL of one animal subjected to TRIO. (d) Quantification of the total number of mCherry $^+$  neurons in the IL following TRIO tracing in experimental and control animals. N=2 (Ctrl), 5 (TRIO) mice/group. (e) Schematic representation (top) and example pictures (bottom) of TRIO controls that did not receive AAV8-DIO-RG-GFP injections in the NRe. Data are represented as mean  $\pm$  SEM. BLA, basolateral amygdala; IL, infralimbic cortex; NRe, nucleus reunions of the thalamus; RG, rabies protein G.



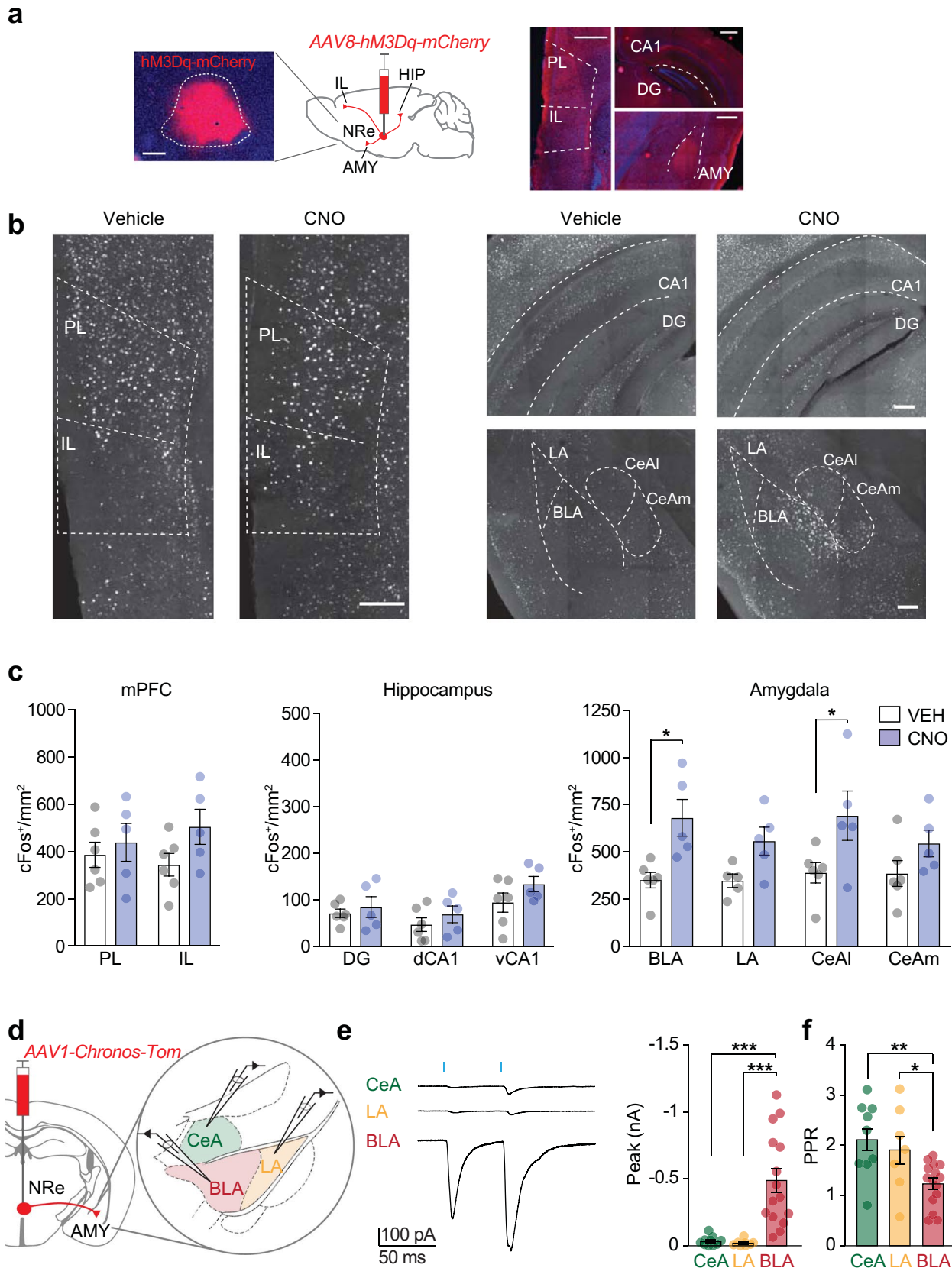
**Extended Data Fig. 4 | Chemogenetic inhibition of the NRe induces persistent extinction impairment and is not due to unspecific CNO effects.** (a) Freezing responses (bottom) during the remote fear memory extinction paradigm (top) upon hM4Di/CNO inhibition of the NRe. Yellow bars indicate CNO administration during extinction but not at recall or SR. Control animals were injected with a homologous virus lacking the hM4Di sequence (AAV8-hSyn::mCherry) and received CNO administration identical to experimental animals. Two-way RM ANOVA, VEH vs CNO:  $F(1, 19)=7.047$ ,  $P=0.0156$ , multiple comparison, Sidak, \*  $P < 0.05$ ;  $N=8$ (hM4Di), 13 (mCherry) animals/group. (b) Freezing responses (bottom) during the remote fear memory extinction paradigm (top) upon CNO administration in hM4Di or mCherry-injected animals in the NRe. Yellow bar indicates CNO inhibition at SR only. Two-way RM ANOVA, VEH vs CNO:  $F(1, 12)=0.14$ ,  $P=0.72$ ,  $N=6$  (CNO), 8 (VEH) mice/group. (c) Representative picture of hM4Di-mCherry expression (virus: AAV8-hM4Di-mCherry) in a mis-injected animal. Scale bar = 800 μm. Zoom-in 200 μm. (d) Experimental timeline for CNO-mediated inhibition during remote fear memory recall, extinction and SR (top). Freezing responses (bottom) during the remote fear memory extinction paradigm and SR upon hM4Di-mediated inhibition of the NRe or its vehicle control. Yellow bars indicate days of CNO administration. Two-way RM ANOVA, VEH vs CNO:  $F(1, 41)=0.05$ ,  $P=0.82$ ,  $N=11$  (CNO), 28 (VEH) mice/group. BL, baseline freezing; CFC, contextual fear conditioning; CNO, clozapine-N-oxide; NRe, nucleus reuniens of the thalamus; Rec, recall; SR, spontaneous recovery; VEH, vehicle. Data are represented as mean  $\pm$  SEM. Statistical analysis details for each figure panel are reported in Supplementary Table 1.



**Extended Data Fig. 5 | NRe activation during remote fear memory extinction facilitates freezing reduction.** (a) Representative pictures of hM3Dq-mCherry expression (red) and cFos (green) in the NRe upon vehicle or CNO injection. Scale bar = 200  $\mu$ m. (b) Quantification of cFos-positive cell density in the NRe upon vehicle or CNO injection. Unpaired t-test,  $P=0.013$ .  $N=5$  (CNO), 6 (VEH) mice/group. (c) (Top) Experimental timeline: All animals underwent contextual fear conditioning (CFC) and received AAV8-CamKII::hM3Dq-mCherry injection one week later. Thirty days after CFC they underwent memory recall and subsequently the spaced extinction paradigm under CNO or vehicle treatment and were tested for spontaneous recovery (SR) two weeks later. (Bottom) Freezing responses during the remote fear memory extinction paradigm and SR upon hM3Dq/CNO activation of the NRe. Blue bars indicate days of CNO exposure. Two-way RM ANOVA, VEH vs CNO:  $F(1, 10)=4.227$ ,  $P=0.0668$ , multiple comparison, Sidak, \*  $p < 0.05$ ,  $N=6$  mice/behavioral group. (d) Freezing responses (Bottom) during the extinction memory test (ET) and SR (top) upon repeated hM3Dq-mediated home cage activation of the NRe in the absence of both the recall and the spaced extinction behavioral paradigm. Two-way RM ANOVA, VEH vs CNO:  $F(1, 14)=1.18$ ,  $P=0.296$ ,  $N=8$  mice/group. BL, baseline freezing; CFC, contextual fear conditioning; CNO, clozapine-N-oxide; ET, extinction test; NRe, nucleus reuniens of the thalamus; Rec, recall; SR, spontaneous recovery; VEH, vehicle. Data are represented as mean  $\pm$  SEM. Statistical analysis details for each figure panel are reported in Supplementary Table 1.

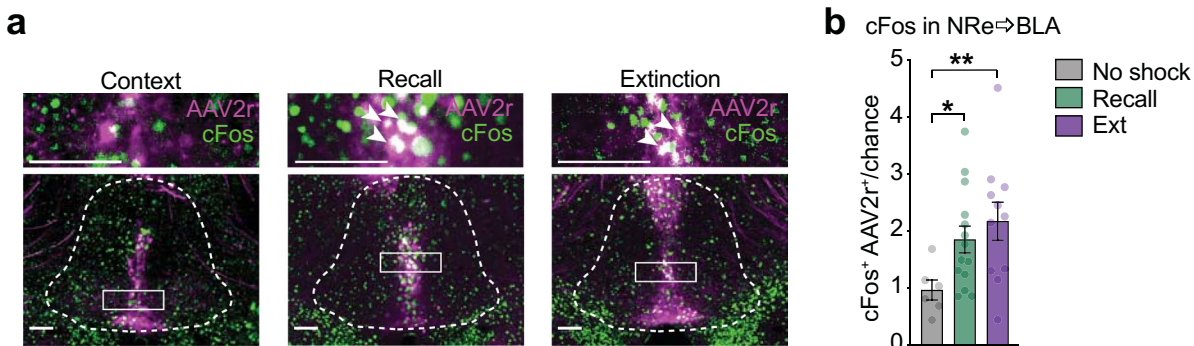
**a****b****c**

**Extended Data Fig. 6 | Activity rise in the NRe starts shortly before freezing cessation throughout remote fear memory extinction and is not time-locked to freezing initiation.** **a,** (Left) Example traces of photometry signals (reported as  $dF/F$ , see Methods) generated by 465 nm (black,  $\text{Ca}^{2+}$ -dependent) and 405 nm (blue,  $\text{Ca}^{2+}$ -independent) LED excitation during the first three days of extinction. Blue boxes indicate freezing bouts ( $0.5 \text{ s} \geq \text{light blue} < 1.5 \text{ s}$ ; dark blue  $\geq 1.5 \text{ s}$ ). (Right) Mean signal  $\pm 2\text{s}$  around cessation of freezing (indicated by the dashed lines) for  $>1.5 \text{ s}$  freezing bouts from the corresponding behavioral session in the left panel. **b,c,** Heat maps represent photometry signals (reported as  $dF/F$ ) for each freezing epoch and the following mobility epoch of one representative recall (**b**), and extinction (**c**), session. All heat maps are aligned to freezing cessation (0s) and ordered by freezing epoch duration. Freezing epochs followed by mobility epochs shorter than 0.1s were excluded from the analysis.

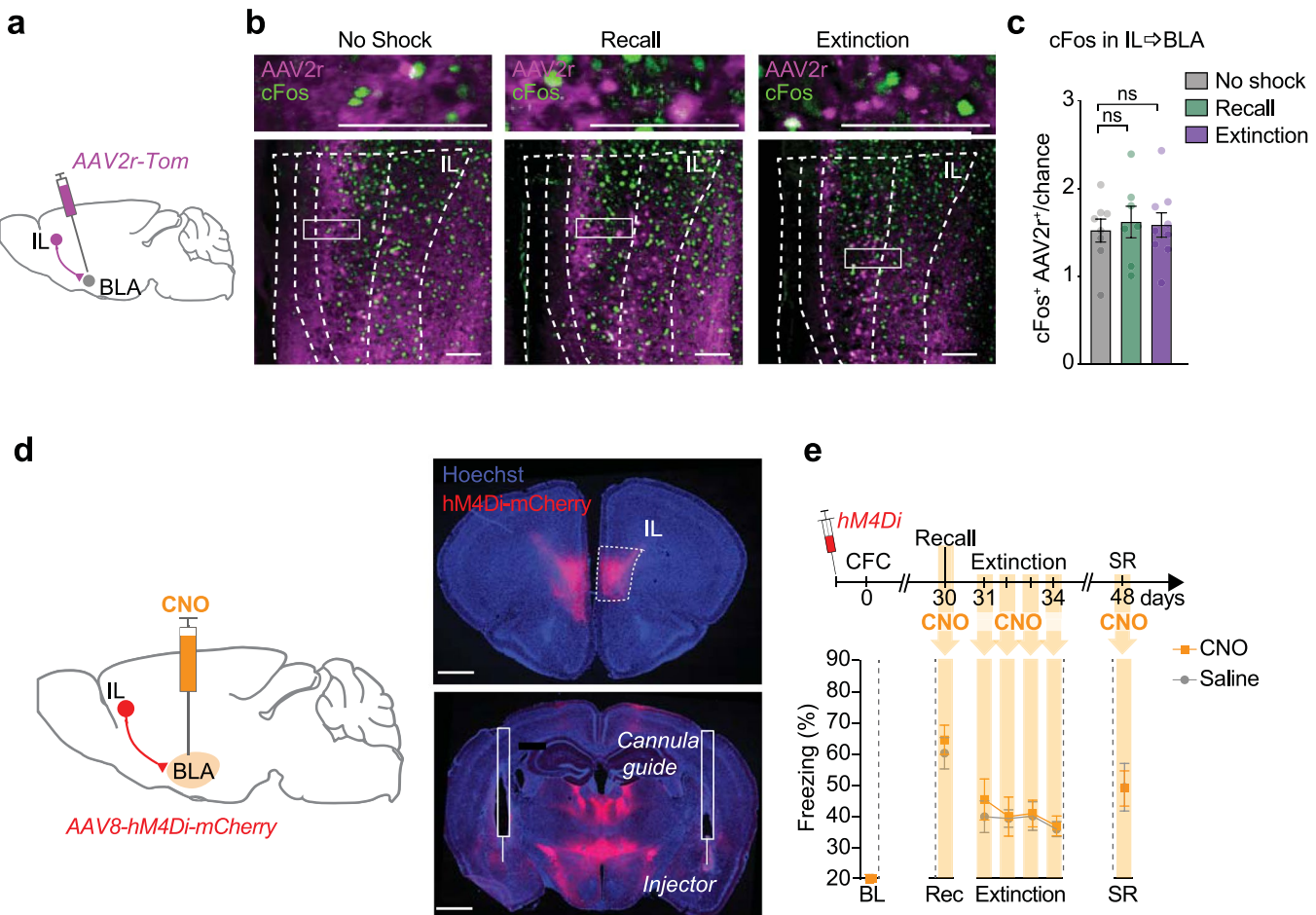


**Extended Data Fig. 7 | See next page for caption.**

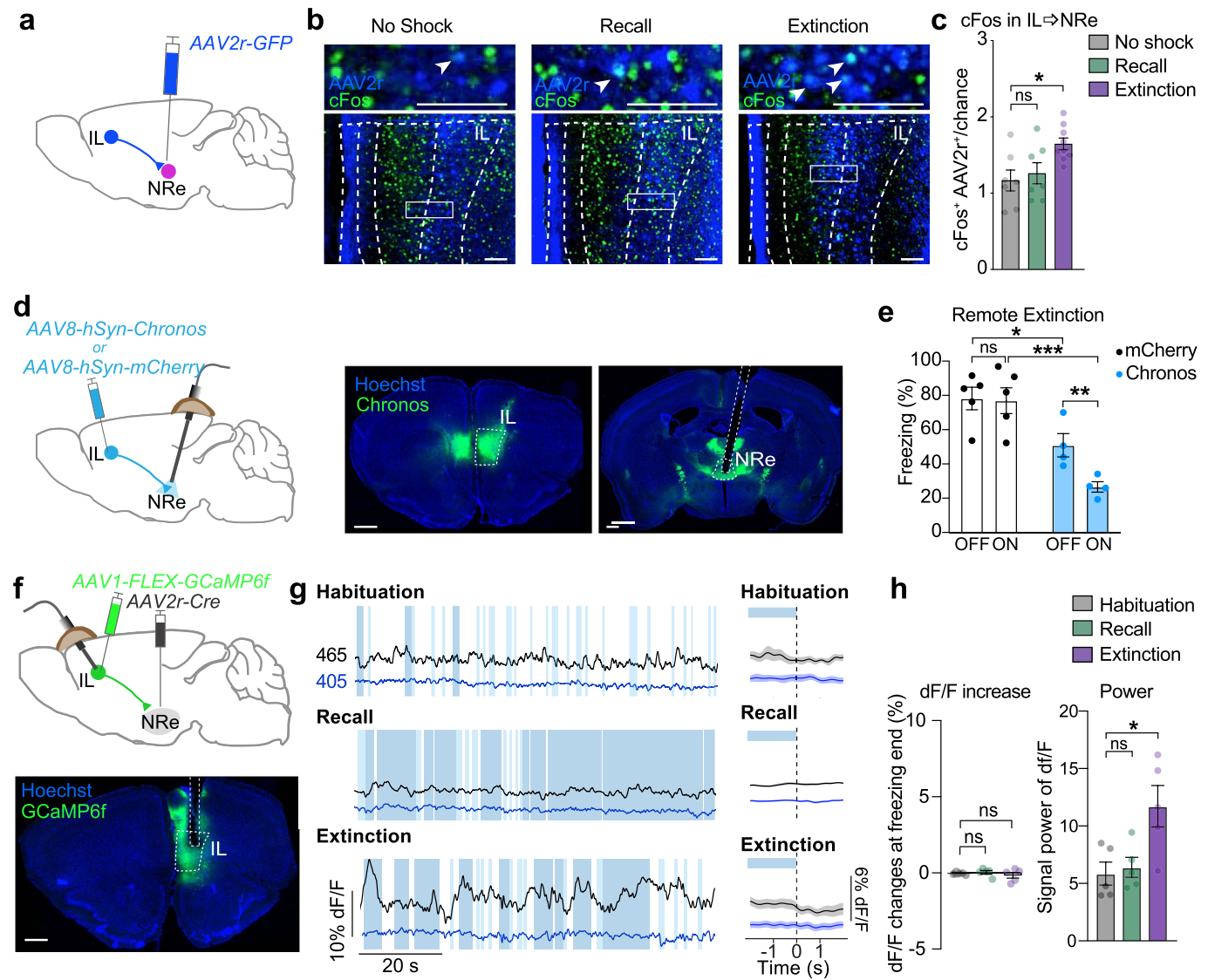
**Extended Data Fig. 7 | Characterization of NRe outputs in behaviorally naïve animals.** **a**, (Left) Schematic representation and representative picture (scale bar = 250  $\mu$ m) of AAV8-CamKII::hM3Dq-mCherry injection in the NRe. (Right) Representative picture of hM3Dq-mCherry axonal expression in the medial prefrontal cortex (mPFC; left, scale bar = 250  $\mu$ m), hippocampus (top-right, scale bar = 250  $\mu$ m) and amygdala (bottom-right, scale bar = 100  $\mu$ m); red=mCherry, blue=Hoechst. **b**, Representative pictures of cFos immunoreactivity in the mPFC (left), hippocampus (top right) and amygdala (bottom right) upon chemogenetic activation of the NRe. Animals were sacrificed 90 min after systemic CNO or vehicle administration. Scale bar 200  $\mu$ m. **c**, Quantification of cFos immunoreactivity following NRe chemogenetic activation in the mPFC, two-way ANOVA, VEH vs CNO: F(1, 18)=2.82, P=0.11, N=5 (CNO), 6 (VEH) mice/group; hippocampus, two-way ANOVA, VEH vs CNO: F(1, 27)=3.17, P=0.09, N=5 (CNO), 6 (VEH) mice/group, and the amygdala, two-way ANOVA, VEH vs CNO: F(1, 35)=22.32, P<0.0001, multiple comparison, Sidak \* P<0.05 N=5 (CNO), 6 (VEH) mice/group. **d**, Schematic representation of AAV1-hSyn::Chronos-Tom injections in the NRe and subsequent ex vivo patch-clamp recordings in neurons of the central amygdala (CeA), and pyramidal cells from the basolateral amygdala (BLA) and the lateral amygdala (LA). **e**, (Left) Representative traces of evoked postsynaptic currents (EPSCs) elicited at -70 mV by brief consecutive LED pulses and (right) values of EPSC peak. One-way ANOVA: F(2, 32)=17.31, P<0.0001; multiple comparison, Holm-Sidak, \*\*\* P<0.001, n=10 (CeA), 8 (LA), 15 (BLA) cells from N=3-6 mice/group. **f**, Paired-pulse ratio (PPR) in the different amygdalar nuclei (color-coded). One-way ANOVA F(2, 28)=7.39, P=0.0026; multiple comparison, Holm-Sidak, \* P<0.05, \*\* P<0.01, n=9 (CeA), 7 (LA), 15 (BLA) cells from N=3-6 mice/group. BLA, basolateral amygdala; CeAl, lateral portion of the central amygdala; CeAm, medial portion of the central amygdala; DG, dentate gyrus; IL, infralimbic cortex; LA, lateral amygdala; mPFC, medial prefrontal cortex; PL, prelimbic cortex. Data are represented as mean  $\pm$  SEM. Statistical analysis details for each figure panel are reported in Supplementary Table 1.



**Extended Data Fig. 8 | cFos activation analysis of NRe→BLA projections during remote fear memory extinction.** **a**, Representative pictures of cFos IHC in retrogradely traced cells from the BLA in the NRe following the remote recall session, the last extinction session and the no shock control group (for the experimental setup see Fig. 1). Scale bar = 100  $\mu$ m. Arrowheads indicate double positive cells in the NRe (AAV2r<sup>+</sup>, cFos<sup>+</sup>). **b**, Colocalization analysis of retrogradely traced cells from the BLA (AAV2r<sup>+</sup>) and cells activated in the NRe (cFos<sup>+</sup>) in the remote recall, extinction and the no shock control group. Kruskal-Wallis test,  $P=0.02$ , multiple comparison, Dunn \*  $P < 0.05$ , \*\*  $P < 0.01$ ,  $N=6$  (No shock), 14 (Recall), 11 (Ext) mice/group; Data are represented as mean  $\pm$  SEM. Statistical analysis details for each figure panel are reported in Supplementary Table 1.



**Extended Data Fig. 9 | cFos activation and functional analysis of IL $\rightarrow$ BLA projections during remote fear memory extinction.** **a**, Schematic representation of the retrograde virus injection strategy. **b**, Representative pictures of cFos IHC in retrogradely traced cells from the BLA in the IL following the remote recall session, the last extinction session and the no shock control group (for experimental setup see Fig. 1). Scale bar = 100  $\mu$ m. **c**, Colocalization analysis of retrogradely traced cells from the BLA (AAV2r $^+$ ) and cells activated in the IL (cFos $^+$ ) in the remote recall, remote extinction and the no shock control group. Kruskal-Wallis test, multiple comparison, Dunn; P = 0.89, N = 8 (No shock), 7 (recall), 9 (Ext) mice/group. **d**, (Left) Schematic representation of the experimental strategy for DREADD-mediated manipulation of IL-deriving terminals in the BLA. (Right) Representative picture of hM4Di-mCherry expression at the level of the injection site in the IL (top) and cannula placement in the BLA (bottom). Notably, hM4Di-mCherry $^+$  fibers can be observed in the NRe and BLA (scale bar = 500  $\mu$ m). **e**, Selective hM4Di-mediated inhibition of IL-deriving terminals in the BLA does not affect remote fear memory extinction. Yellow bars indicate local BLA infusions of CNO/VEH at remote recall and throughout the remote fear memory extinction paradigm. Two-way RM ANOVA, VEH vs CNO: F(1, 7)=0.234, P=0.643, multiple comparison, Sidak, N=4 (VEH), 5 (CNO) mice/group. Data are represented as mean  $\pm$  SEM. Statistical analysis details for each figure panel are reported in Supplementary Table 1.



**Extended Data Fig. 10 | Functional characterization of IL→NRe projections during remote fear memory extinction.** **a**, Schematic representation of the retrograde virus injection strategy. **b**, Representative pictures of cFos IHC in retrogradely traced cells from the NRe in the IL following the remote recall session, the last extinction session and the no shock control group (for experimental setup see Fig. 1). **c**, Colocalization analysis of retrogradely traced cells from the NRe (AAV2r<sup>+</sup>) and cells activated in the IL (cFos<sup>+</sup>) in the remote recall, remote extinction and the no shock control group. Kruskal-Wallis test,  $P=0.031$ ,  $N=7$  (No shock), 7 (recall), 9 (Ext) mice/group; multiple comparison, Dunn, \*  $P < 0.05$ . Arrowheads indicate double positive cells in the IL (AAV2r<sup>+</sup>, cFos<sup>+</sup>). **d**, Schematic representation (left) and representative pictures (right) of the viral strategy for optogenetic stimulation of IL→NRe projections. AAV8 vectors carrying the activatory opsin Chronos-mCherry or mCherry only were injected bilaterally in the IL and an optic fiber was implanted above the NRe. Scale bar = 500  $\mu$ m. **e**, Freezing behavior quantification upon optogenetic stimulation (20 Hz, 5 s light ON, 5 s light OFF, total duration=3 min) of IL→NRe projections during one remote fear memory extinction session. Two-way ANOVA for freezing time during light ON and OFF periods during one remote extinction session, interaction:  $F(1, 7)=17.42$ ,  $P=0.0042$ ; ON vs OFF:  $F(1, 7)=21.49$ ,  $P=0.0024$ , multiple comparison, Sidak, \*  $P < 0.05$ , \*\*  $P < 0.01$ , \*\*\*  $P < 0.001$ .  $N=4$  (Chronos), 5 (mCherry) mice/group. **f**, Schematic representation of the experimental approach and fiber photometry recording implant for IL→NRe fiber photometry recordings (top); representative picture of GCaMP6f expression and localization of the optical fiber implant in the IL (bottom). Scale bar = 500  $\mu$ m. **g**, (Left) Example traces of photometry signals (reported as df/F, see Methods) generated by 465 nm (black,  $\text{Ca}^{2+}$ -dependent) and 405 nm (blue,  $\text{Ca}^{2+}$ -independent) LED excitation during habituation, recall and the last extinction session. Blue boxes indicate freezing bouts ( $0.5 \text{ s} \geq \text{light blue} < 1.5 \text{ s}$ ; dark blue  $\geq 1.5 \text{ s}$ ). (Right) Mean df/F signal  $\pm 2$  s around cessation of freezing (indicated by the dashed line, 0 s) for  $\geq 1.5 \text{ s}$  freezing bouts from the corresponding behavioral session in the left panel. **h**, (Left) Quantification of df/F difference before and after freezing end. RM One-way ANOVA,  $F(2, 8)=0.989$ ,  $P=0.41$ , multiple comparison, Holm-Sidak,  $N=5$  animals. (Right) Signal power analysis of df/F during remote fear memory extinction. Signal power was calculated as  $\Sigma(\text{df}/\text{F}-\text{av. df}/\text{F})^2$ . RM One-way ANOVA,  $F(2, 8)=6.72$ ,  $P=0.019$ , multiple comparison, Sidak, \*  $P < 0.05$ .  $N=5$  animals. Data are represented as mean  $\pm$  SEM. Statistical analysis details for each figure panel are reported in Supplementary Table 1.

Corresponding author(s): Johannes Gräff

Last updated by author(s): 2021/03/05

## Reporting Summary

Nature Research wishes to improve the reproducibility of the work that we publish. This form provides structure for consistency and transparency in reporting. For further information on Nature Research policies, see [Authors & Referees](#) and the [Editorial Policy Checklist](#).

### Statistics

For all statistical analyses, confirm that the following items are present in the figure legend, table legend, main text, or Methods section.

n/a Confirmed

- The exact sample size ( $n$ ) for each experimental group/condition, given as a discrete number and unit of measurement
- A statement on whether measurements were taken from distinct samples or whether the same sample was measured repeatedly
- The statistical test(s) used AND whether they are one- or two-sided  
*Only common tests should be described solely by name; describe more complex techniques in the Methods section.*
- A description of all covariates tested
- A description of any assumptions or corrections, such as tests of normality and adjustment for multiple comparisons
- A full description of the statistical parameters including central tendency (e.g. means) or other basic estimates (e.g. regression coefficient) AND variation (e.g. standard deviation) or associated estimates of uncertainty (e.g. confidence intervals)
- For null hypothesis testing, the test statistic (e.g.  $F$ ,  $t$ ,  $r$ ) with confidence intervals, effect sizes, degrees of freedom and  $P$  value noted  
*Give P values as exact values whenever suitable.*
- For Bayesian analysis, information on the choice of priors and Markov chain Monte Carlo settings
- For hierarchical and complex designs, identification of the appropriate level for tests and full reporting of outcomes
- Estimates of effect sizes (e.g. Cohen's  $d$ , Pearson's  $r$ ), indicating how they were calculated

*Our web collection on [statistics for biologists](#) contains articles on many of the points above.*

### Software and code

Policy information about [availability of computer code](#)

Data collection

TSE, Multi-conditioning System, automatic freezing detection; pClamp 10 (Clampex10, v10.6), Molecular devices, ex vivo electrophysiology; Doric Neuroscience Studio, Doric Lenses, fiber photometry data acquisition.

Data analysis

Igor Pro8, WaveMetrics and R studio, fiber photometry data visualization and data analysis; QuPath v1.3 and v. 1.4, Image J (Fiji v2.1.0) image analysis; GraphPad Prism 6-8, data plotting and statistical analysis; Clampfit10, Molecular Devices v10.6 for patch clamp recordings analysis;

For manuscripts utilizing custom algorithms or software that are central to the research but not yet described in published literature, software must be made available to editors/reviewers. We strongly encourage code deposition in a community repository (e.g. GitHub). See the Nature Research [guidelines for submitting code & software](#) for further information.

### Data

Policy information about [availability of data](#)

All manuscripts must include a [data availability statement](#). This statement should provide the following information, where applicable:

- Accession codes, unique identifiers, or web links for publicly available datasets
- A list of figures that have associated raw data
- A description of any restrictions on data availability

The data that support the findings of this study are available from the corresponding author upon request. All code used in the manuscript is available at <https://zenodo.org/record/4588295>

# Field-specific reporting

Please select the one below that is the best fit for your research. If you are not sure, read the appropriate sections before making your selection.

- Life sciences       Behavioural & social sciences       Ecological, evolutionary & environmental sciences

For a reference copy of the document with all sections, see [nature.com/documents/nr-reporting-summary-flat.pdf](https://nature.com/documents/nr-reporting-summary-flat.pdf)

## Life sciences study design

All studies must disclose on these points even when the disclosure is negative.

Sample size	No statistical methods were used to pre-determine sample sizes. Sample sizes used were based on previous publications performing similar experiments (Silva et al., 2019; Khalaf et. al 2018)
Data exclusions	Animal were excluded from further experimentation or data analysis if they displayed: cannula or optic fiber implant loss or infection; misplaced stereotaxic injections or poor viral expression
Replication	All experiments were independently replicated in at least 2 cohorts of animals (n number of each experimental group is reported in every figure legend). Image analysis of cFos/AAV2r colocalization was independently replicated by different experimenters.
Randomization	Mice were raised and housed in the same conditions and randomly allocated to the different experimental groups.
Blinding	The investigators were blinded to the experimental group for sample processing, image analysis and behavioral analysis.

## Reporting for specific materials, systems and methods

We require information from authors about some types of materials, experimental systems and methods used in many studies. Here, indicate whether each material, system or method listed is relevant to your study. If you are not sure if a list item applies to your research, read the appropriate section before selecting a response.

Materials & experimental systems	Methods
n/a	Involved in the study
<input type="checkbox"/>	<input checked="" type="checkbox"/> Antibodies
<input checked="" type="checkbox"/>	<input type="checkbox"/> Eukaryotic cell lines
<input checked="" type="checkbox"/>	<input type="checkbox"/> Palaeontology
<input type="checkbox"/>	<input checked="" type="checkbox"/> Animals and other organisms
<input checked="" type="checkbox"/>	<input type="checkbox"/> Human research participants
<input checked="" type="checkbox"/>	<input type="checkbox"/> Clinical data
n/a	Involved in the study
	<input checked="" type="checkbox"/> ChIP-seq
	<input checked="" type="checkbox"/> Flow cytometry
	<input checked="" type="checkbox"/> MRI-based neuroimaging

## Antibodies

Antibodies used	Rabbit polyclonal anti-cFos, Synaptic System, Cat# 226 003, RRID:AB_2231974; Rabbit Anti-NeuN antibody, 1:1000, Merk, #ABN78, ,Alexa Fluor 647-conjugated donkey anti-rabbit IgG (Invitrogen, # A-31573)
Validation	The specificity of the antibody have been validated by the manufacturers. A list of scientific publications about antibody validation in the mouse brain can be found on the manufacturers website. References list for 226003 anti-cFos validation can be found at <a href="https://sysy.com/product/226003">https://sysy.com/product/226003</a> . References list for ABN78 anti-NeuN validation can be found at <a href="https://www.merckmillipore.com/CH/en/product/Anti-NeuN-Antibody-rabbit,MM_NF-ABN78#anchor_REF">https://www.merckmillipore.com/CH/en/product/Anti-NeuN-Antibody-rabbit,MM_NF-ABN78#anchor_REF</a>

## Animals and other organisms

Policy information about [studies involving animals](#); [ARRIVE guidelines](#) recommended for reporting animal research

Laboratory animals	Mus musculus, C57BL/6JRj, 5-7 week old (surgeries), males, 8-16 weeks old (behavioral testing).
Wild animals	The study did not involve wild animals
Field-collected samples	The study did not involve samples collected from the field
Ethics oversight	The federal Food Safety and Veterinary Office of the Federal Council of Switzerland approved the animals licenses VD2808 and VD2808.1 for the experiments performed in this study.

Note that full information on the approval of the study protocol must also be provided in the manuscript.